Ca' Foscari
University
of Venice

Master's Degree programme in

Science and Technology of Bio and Nanomaterials

Low Band Gap Nanostructures for Electrocatalysis

Supervisors

Prof. Elisa Moretti

Prof. Alberto Vomiero

Assistant supervisor

Dr. Kamran Akbar

Graduand

Edlind Lushaj

858925

Academic year

2020/2021

Abstract

Nowadays, the development of novel oxygen evolution reaction (OER) electrocatalysts with high performances and low costs for a large-scale application in water splitting is challenging. To settle such issue, herein, a facile route based on nickel hexacyanoferrate (Ni-HCF) and cobalt hexacyanoferrate (Co-HCF) nanostructures was developed to fabricate selenized Ni-HCF and Co-HCF core-shell nanocubes for OER in alkaline electrolyte. The obtained electrocatalysts were characterized by UV-Vis, XRD, SEM, EDS and FTIR methods, and their catalytic activity was then evaluated by electrochemical technique. The core-shell selenized Ni-HCF and Co-HCF nanocubes exhibited an excellent OER electrocatalytic activity with a very low overpotential of 160 mV and 280 mV (vs RHE), which are much lower than that of bare Ni-HCF (onset overpotential of 280 mV) and Co-HCF (onset overpotential of 350 mV), respectively. The core-shell nanocubes also exhibit a very small Tafel slope of 33 mV/dec for the selenized Ni-HCF sample and 99 mV/dec for the selenized Co-HCF sample. The excellent electrocatalytic performance of these samples can be assigned to their hierarchical structure, which significantly speed up the kinetics of the reaction. This thesis offers a facile synthesis strategy for selenium-based transition metal hexacyanoferrate catalysts with excellent electrocatalytic efficiency towards OER.

INDEX

1. General introduction

1.1 Overview on electrocatalysis

Electrocatalysis started to grow as a field of electrochemistry in the late eighties due to the application of new techniques[1]. However, in the earlier stages of this field most of the applications were involved in academic purposes but not for use in the industry. Nowadays instead, the application of new concepts of electrocatalysis for industrial electrochemical processes has appeared as a necessity in response to increasing energy demand and not only arising the interest for researchers[2]. Therefore, electrocatalytic processes have only been presented in the literature from a general point of view with few further electrochemical explanations. The design and preparation of an electrocatalyst are based on new concepts such as a controlled surface, morphology, well-defined catalytic sites, and mechanisms during the electrochemical reactions[3].

Electrocatalysis can be described as an electrochemical reaction with an adsorbed species which can influence the kinetics as well as the mechanism of the reaction[4]. Although the concept of electrocatalysis is mainly related to an experimental field of electrochemistry, the advances in theory and the development of new electrocatalysts are the main keys for the advancement of the field.

The fast advances in electrocatalysis made scientists need advanced techniques to understand the principles and the mechanisms of such processes and to develop more efficient electrocatalysts. Some combined techniques (e.g. differential electrochemical mass spectrometry)[5] show the possibility of continuous analyses of an electrode reaction with the detection of volatile or gaseous products in the course of the electrochemical reaction. In fact, differential electrochemical mass spectrometry studies allowed to observe that carbon support degradation, distribution of products, and catalytic activity towards compounds such as carbon dioxide depend significantly on the surface chemistry[6].

There are many applications of electrocatalysis for technological electrochemical reactions[7], organic electrosynthesis[8], electrode sensors[9], fuel cells[10], batteries[11], and so on. Electrocatalysts for energetic applications are presented in this thesis to give an insight into the possibilities of this science. These applications seem to be the main ones since they yield long-lasting experiments without contamination or poisoning of the electrode surfaces.

1.2 Fundamentals of electrocatalysis

Electrochemical reactions can be separated into oxidation reactions and reduction reactions and can take place in separate compartments[12]. These reactions occur at the surface of electrodes by the exchange of electrons between the reactant and the electrode. In this configuration, two different processes occur

at the same time. Electrons move through the electrical circuit where they can do electrical work or gain electrical energy. Simultaneously, ions move through the electrolyte between the two compartments to maintain a neutral charge[13].

The energy efficiency could be improved minimizing losses due to the resistance according to Ohm's law (Eq.1):

$$\Delta U = R \cdot I \qquad \text{Eq. 1}$$

where ΔU represents the voltage drop, R the resistance, and I the current. The loss in power is given by the product of ΔU and I, so ΔU must be minimal, which requires R to be small. Moreover, R is proportional to the distance between the electrodes and so the distance should be minimized. In addition to the contribution of the distance between the electrodes, the resistance inside the electrodes and the choice of the electrolyte material as well are fundamental[14]. The principle of minimization of energy losses applies to all electrochemical devices[15] working at high power and current densities, for instance, fuel cells[16] and supercapacitors[17]. In addition, from the previously reported Ohm's law it can be seen that the voltage loss and the power loss of an electrochemical cell are directly proportional to the current at which the cell is operating.

Also, the effect of applying an electrical potential must be taken into account. In fact, the application of potential influences the nature of the species adsorbed onto the electrodes, as well as the energy of the bonds between the species and the surface of the electrode[18]. Chemical bonds and/or van der Waals interaction usually stabilize the adsorbate at the surface of the electrode[19]. These kinds of interactions are affected by an applied bias since it could lead to a block of the surface of other adsorbates formed during the process such as intermediates or by-products[20]. Furthermore, the application of higher potentials could make the products able to bind to the surface for a sufficient amount of time to react and give new products.

On the nature of the electrode, it can be said that it is a catalytic reaction partner that undergoes specific interactions with adsorbates. The product of the catalyzed reaction depends on the chemical composition and the microstructure of the electrode surface in a similar way as it is well known for conventional heterogeneous catalysts. The possibility of obtaining different products and the dependence of the outcome of the experiment based on the nature of the catalyst was demonstrated by a massive number of researches[21], [22]. In addition to this, it was observed that specific interactions are present, even if little information is known about them.

Among the multitude of chemical reactions, only those that can be divided into oxidation and a reduction can be led electrochemically. The reactants must be able to undergo an electron exchange with suitable electrodes and this severely affects electrochemical reactions. However, electrocatalysis has also many advantages. For instance, exergonic processes allow converting chemical energy into electrical energy. Moreover, the energy needed for endergonic processes can be supplied in the form of electrical energy, allowing in this way endergonic processes to take place at room temperature[23]. The rates of the reactions could be also controlled by varying the current in the circuit.

1.3 Essential parameters for a good electrocatalyst

The most valuable characteristics of an electrocatalyst are high activity, stability, and selectivity. The activity of an electrocatalyst is determined by different parameters[24]. The most important ones are overpotential at a defined areal current density (usually at 10 $m \cdot A \cdot cm^{-2}$); overpotential at a defined mass normalized current density; overpotential at a defined electrochemical surface area (ECSA) normalized current density; Tafel slope; exchange current density; and turnover frequency (TOF)[25].

The last three kinetic parameters describe how fast the reaction is. Overpotential, defined as the difference between the theoretical thermodynamic and real electrode reduction voltages, should be as low as possible[26]. Similarly, mass activity is used sometimes by researchers as well to show the loading effect.

Tafel slope (Eq. 2) is the kinetic parameter obtained from the plot – known as Tafel plot – of the logarithm of the current density against the overpotential[27]. The Tafel slope is inversely proportional to the charge transfer coefficient (α) and the number of electrons transferred in the electrocatalytic reaction. So, the Tafel slope must be kept low for a given electrocatalyst[28].

$$\text{Tafel slope} = 2.303\, RT/\alpha nF \qquad \text{Eq. 2}$$

Exchange current density, instead, is found by the extrapolation of the linear portion of the Tafel curve until it does intersect at the point where the equilibrium potential of the electrocatalytic process meets the respective current density. The parameter extrapolated in this way is the exchange current density. A good electrocatalyst possesses high values of exchange current density. TOF is also another kinetic activity parameter. TOF is simply the measure of the amount of hydrogen and oxygen generated per unit of time. Also, in this case, TOF's value should be as high as possible for a good electrocatalyst[29].

The stability of an electrocatalyst is a key parameter that determines the chance to scale up the electrocatalyst's application to a large scale[30]. A good electrocatalyst should always perform at catalytic

turnover conditions. In hydrogen evolution reaction (HER) and oxygen evolution reaction (OER) electrocatalysis, the stability of an electrocatalyst can be tested by rapidly cycling of the catalyst electrode within the experimental potential range and observing the trend of the over-potential during the cycling and, alternatively, by prolonged potentiostatic or galvanostatic electrolysis. In general, a catalyst is categorized as stable if the overpotential does not increase more than 30 mV and the activity degradation after the tests is not more than 5%. Moreover, a lot of attention must be given to the catalyst fixation method and the selection of the electrode's substrate since they influence the stabilization of the electrocatalyst.

Similarly, the selectivity of the electrocatalyst is crucial for enhancing energy efficiency. The electrical energy applied to the system must be exclusively used for the electrocatalytic process. However, this is the challenge of OER electrocatalysis in which many side reactions (i.e. formation of ozone, hydrogen peroxide, and hydrogen superoxide) take place. In addition, the catalytic sites must undergo a continuous cycle of oxidation and reduction as well. Inevitably, part of the energy provided to the system is used for these side reactions contributing to the overall energy loss during the process. Faradaic efficiency (FE) calculation is the only method to determine the selectivity of a given electrocatalyst[31]. This parameter can be determined using: gas chromatography, for both HER and OER; and rotating ring disk electrode (RRDE), for OER only[32]. To become feasible as a commercial water electrolyzer, a performant electrocatalyst should have a FE of at least 90%[33].

These characteristics are introduced to understand the activity of the proposed electrocatalysts as efficient materials for electrocatalytic water splitting applications.

1.4 Water splitting, HER and OER

Splitting of pure water electrochemically requires a huge input electrical energy as the resistance of pure water is 18 M·Ω·cm[34]. Usually, researchers perform water electrolysis in extremely acidic electrolytes (pH 0) with inert anions (e.g. sulfate and perchlorate) or in extremely basic electrolytes (pH 14) (e.g. KOH and NaOH). Equations (i) and (ii) are the half-cell reactions for HER and OER in acidic conditions, respectively; while equations (iii) and (iv) are the half-cell reactions for HER and OER in basic conditions, respectively.

(i) $4H^+ + 4e^- \rightarrow 2H_2$ $E°=0.0V$

(ii) $2HO \rightarrow O + 4H^+ + 4e^-$ $E°=+1.23V$

(iii) $4H_2O + 4e^- \rightarrow 2H_2 + 4OH^-$ $E°=-0.828V$

(iv) $4OH^- \rightarrow O_2 + H_2O + 4e^-$ $E°=+0.401V$

According to the equations reported above, the minimum cell voltage required to split water into hydrogen and oxygen regardless of the medium is 1.23 V. Like all electrochemical redox reactions, electrochemical (EC) water splitting (WS) embraces the Nernst equation, hence showing strong pH dependence[35] as it can be seen in **Figure 1**[36]:

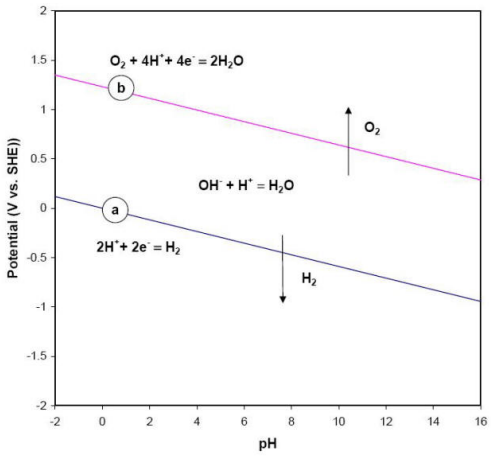

Figure 1. Pourbaix diagram of water showing the pH dependence of OER and HER[36].

From **Figure 1**, it is clear that in a fuel cell the electrolysis of water cannot be achieved without applying 1.23 V[37].

However, there are other thermodynamic parameters that disallow the manifestation of water splitting at 1.23 V. One of the possible thermodynamic factors affecting the process is the energy that has to be supplied for increasing entropy of the system.

It has been calculated and predicted that a cell voltage of 1.481 V is needed to begin sustained WS in which the electrochemical cell will not withdraw heat from the surroundings. This potential is called the thermoneutral potential of water splitting[37]. Unfortunately, there is no way to split water electrochemically without losing a significant amount of energy[38]. In this regard, the energy loss in EC WS can be lowered through a rational design of highly performant electrocatalysts able to deliver high catalytic current densities.

As mentioned before, electricity-driven water splitting is composed of two half-cell reactions separated by a membrane (**Figure 2**[39]).

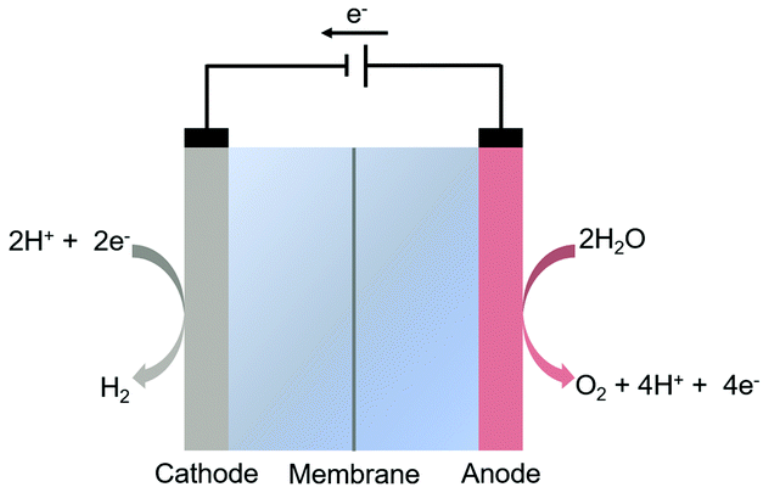

Figure 2. Pictorial representation of electrochemical water splitting[39].

The reduction process that takes place at the cathode is the hydrogen evolution reaction (HER), while the oxidation process occurring at the anode is the oxygen evolution reaction (OER). To understand how this electrocatalytic process works, it is important to understand the mechanism of HER and OER.

HER. HER is a process that starts with the adsorption of a proton or a molecule of water on the catalytic site, which proceeds to discharge the adsorbed species. After that, the discharged proton may combine with other discharged protons to generate a hydrogen molecule or it may get attached to another proton that has to undergo discharge.

There are two mechanisms in HER: Tafel[40] and Volmer–Heyrovsky mechanisms[41]. Tafel mechanism is the most straightforward method since it consists of three steps[42] and it can be described as follows:

$$M + H^+ \rightarrow M\text{-}H^+$$

$$M\text{-}H^+ + e^- \rightarrow M\text{-}H$$

$$2M\text{-}H \rightarrow H_2\,(g) + 2M$$

Where M is used to represent a metal surface atom. The mechanism of HER is usually predicted using Tafel slope's values. If the kinetics of the reaction are fast, the Tafel slope will be lower. The slopes of the curves can be observed in the range of 25–35 mV dec^{-1} for HER and in this case, they are said to follow the Tafel pathway, while all the other possible Tafel slopes values greater than 40 mV dec^{-1} are said to follow the Volmer–Heyrovsky mechanism.

OER. In the case of OER, several mechanisms have been proposed for both acidic and alkaline conditions. Among the various mechanisms proposed, the most widely accepted are electrochemical

oxide/oxide pathways[43]. An electrochemical oxide pathway in acidic conditions that is widely accepted for OER mechanism is reported:

$$2M\text{-}OH \rightarrow M\text{-}O + M + H_2O$$

$$2M\text{-}O \rightarrow 2M + O_2\ (g)$$

This mechanism has been shown to fit well with the experimental results of many simple catalysts (e.g. oxides), but discrepancies were observed with more complex structures.

Differently from HER, OER requires the catalytic site to undergo a continuous cycle of oxidation and reduction from the adsorption of water molecule/OH^- to the evolution of O_2. This implies that the material undergoes structural reorganization at the surface to provide the active structure at the catalytic site. Amorphous electrocatalysts offer the required flexibility for this kind of structural reorganization, while crystalline ones are more unlikely to undergo such processes[43].

From the comparison of HER with OER, it is worth noting that OER is kinetically slower because OER is a four-electron transfer reaction, while HER is a two-electron transfer reaction[44]. Therefore, it is clear that OER is the key process that influences the efficiency of electrochemical water splitting. To date, Ir- and Ru- electrocatalysts have been state-of-the-art OER catalysts, but both of them are precious metals with a high cost. Therefore, research is focusing on the production of low-cost alternative materials that can reduce the kinetic issue of OER and, subsequently, improve the overall efficiency in the water-splitting process.

The electrocatalyst's performance in OER is affected by the number of active sites and by their intrinsic activity. According to the number of active sites, reducing the particle size, engineering catalyst morphology, and promoting the surface reconstruction of the catalysts into the active species are the main approaches used to increase the exposure of the active sites themselves[45]. To improve the activity of the active site that enables OER at potentials close to the thermodynamic limit, instead, there is the need to understand deeply the reaction mechanisms and find the origin of the overpotential that generates at the active site of different materials. Many reaction mechanisms have been proposed and according to them, it is possible to rationally design more performant OER electrocatalysts.

1.5 Prussian Blue Analogues

Concerning Prussian blue analogs (PBAs), they have been studied and applied in various fields for a long time. They were first synthesized in Berlin as synthetic pigments in the early 18th century[46].

Subsequently, also thanks to improved knowledge of these materials, many other applications were developed, for instance, energy storage[47] and environmental requalification [48]. In addition, they display high activity as a catalyst for water oxidation and can be utilized as biosensors and as cathode materials[49].

PBAs can display several advantages when used as energy storage materials: i) the open frameworks provide 3D diffusion channels for diffusion of various charge-carrier ions[50]; ii) control over the composition can be achieved for optimization of PBA materials with negligible change in the overall structure[51]; iii) the open framework structure of PBAs results in high stability of PBA-based electrodes[52], and iv) the relatively low-cost of PBAs is suitable for large-scale applications[53].

Besides, PBA materials have been studied as cathodes in supercapacitor applications such as for Li^+-ion storage, Na^+-ion storage, etc[54].

However, some challenges impair the further development of PBA materials and their practical applications: i) the $[Fe(CN)_6]$ vacancies and the coordinated water molecules in the framework of PBA materials reduce their crystallinity, decreasing the overall performance[55] ii) side reactions such as oxygen evolution reactions occur due to the narrow electrochemical window of aqueous electrolytes; iii) the electrochemical reaction mechanisms of the PBA cathodes is complicated and varies according to variation in the composition and/or the electrolyte systems[56].

Recently, several signs of progress on the research of PBAs have been achieved, among which some focus on the applications of PBAs as electrochemical catalysts. Novel potential applications and strategies to optimize them in energy storage and conversion technologies involving the construction of more complex structures, novel morphologies, and composite systems have been reported[57].

The electrochemical performances of the electrodes are closely related to the structure of such materials. The basic Prussian blue material, $Fe_4[Fe(CN)_6]_3 \cdot nH_2O$, has a face-centered cubic phase[58]. Divalent and trivalent Fe atoms alternate in the face-centered cubic structure connected by -C≡N- bonds. Among them, Fe^{2+} and Fe^{3+} ions are surrounded by C and N to form octahedrons, respectively. To maintain electrical neutrality, the ratio between Fe^{2+} and Fe^{3+} ions should be maintained at about 3:4. As a result, there exist ~25% vacancies in the $[Fe(CN)_6]^{4-}$ sites, that will be filled by H_2O molecules. Two types of structural water molecules can be present: one is coordinated water in the empty nitrogen sites with six water molecules coordinated to Fe(III); the other contains interstitial water (up to a maximum of 8 molecules) which can fill in the center of the unit cell or connect with the hydrogen bonds to the

coordinated ones. The latter type of structural water can strongly affect electrochemical performance. Therefore, a single PB unit cell can contain up to 14 water molecules[59].

Changing the composition of PBA materials, their crystal structure can be tuned. Generally, there exist three types of crystal structures for PBA materials: cubic-type, monoclinic-type, and rhombohedral-type structures[60]. PBA materials possess the following chemical formula:

$$A_xP[R(CN)_6]_{1-y}\ Y_y \cdot nH_2O$$

where A is the alkali metal or alkaline earth metal, P and R represent the transition metals, Y is the $[R(CN)_6]$ vacancies, and $0 \leq x \leq 2$, $y < 1$. The nitrogen-coordinated P cations and carbon-coordinated R cations are in an open framework bridged by cyanide groups (-CN-), as reported schematically in **Figure 3** [60].

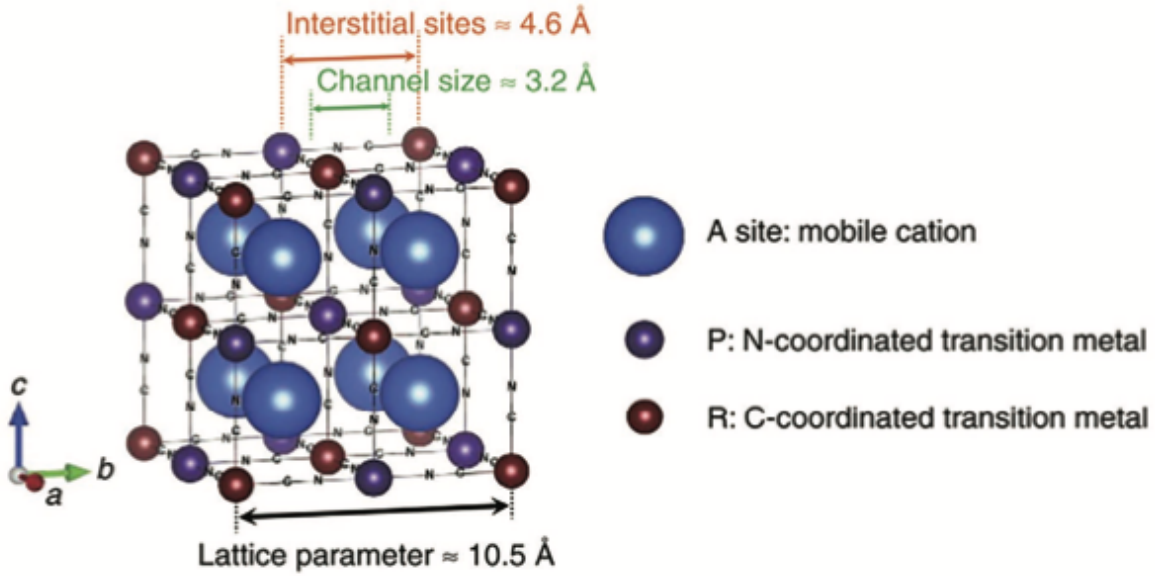

Figure 3. Schematic illustration of $A_xP[R(CN)_6]_y \cdot nH_2O$ materials (A = alkali metal or alkaline earth metal, P and R represent the transition metals in different locations)[60].

The alkali metal ions or alkaline earth metal ions are usually inserted, while the transition metals replace the $Fe^{2+/3+}$ sites. Thus, it is clear that different PBA materials can be developed with optimized electronic and ionic properties for enhancing electrode performance. The open-framework nature of PBA structures - containing open channels and interstitial sizes - enables the diffusion of various carrier ions. Here, both the N-coordinated and C-coordinated transition metals are active from an electrochemical point of view[60].

1.6 Selenization

The metal chalcogenides form an almost infinite class of materials. The efforts put in this area are driven by technological applications of these materials as well as their remarkable diversity in structure and properties[61]. Among them, transition metal chalcogenide (TMC) and transition metal dichalcolgenide (TMD) materials have arose the interest of the scientific community, because of their superior mechanical, electrical and optical properties different from their bulk counterparts.

The initial investigations on such materials were driven by research in terms of their attractive properties, but in recent years this interest shifted towards more studies oriented to their application. For instance, TMCs and TMDs are often the building blocks for the production of functional devices and novel electronics[62]. Therefore, they are promising candidates for current technologies such as renewable energy and quantum computing.

However, to scale up their production, efficient and low-cost methods are needed in order to take advantage of their outstanding physical and chemical properties. The production methods consist of two opposite directions. Firstly, starting from molecular precursors (bottom-up)[63] and secondly starting from bulk layered materials (top-down)[64]. Bottom-up methods organize small molecules into single- or few-layer thin sheets. Usually, the reactions take place at the gas–solid, liquid–solid, or air–liquid interfaces.

This kind of approaches has to deal with complex and costly synthetic procedures. On the other hand, top-down methods, such as exfoliation, extract individual sheets held together by weak van der Waals interactions from the solid crystals. Additionally, the abundant bulk materials allow the use of exfoliation strategies because they are straightforward and low-cost[65]. Furthermore, in top-down approach some parameters can be varied to determine the production rate, the purity and the quantity of exfoliated materials. Other approaches can be liquid-phase sonication or shear-force peeling, but they have many drawbacks such as low yield[66]. All these factors yield to high costs that hinder the production of TMC and TMD materials beyond the laboratorial scale.

Many of the properties and applications of these materials are depending on the synthesis method since it can determine the composition, the phase structure and the morphology.

Traditionally, CVD technique[67], molecular precursors, chemical method, solid-state synthesis[68], ultrasonic synthesis[66], hot-injection[69], hydrothermal[70] and solvothermal[71] process are employed to synthesize chalcogen-based nanomaterials. It is clear that there are many methods for preparing TMCs and TMDs. In a special way, transition metal selenides have gained a lot of attention recently. A wide

range of metal and selenium precursors are used for the synthesis of the selenium-based materials by many researchers. NaHSe, Na_2SeO_3, H_2Se, $Se(C_2H_5)_2$, selenium powder, $Se(TMS)_2$, $H_2NC(Se)NH_2$, and SeO_2 have been introduced for these synthesis. Compared with the commercial Se powder, the produced Se from the reduction of Se^{4+} is much more reactive[72]. Researchers use a surfactant to improve the stability of the suspension against flocculation. The surfactant also reduces the toxicity of the selenide source and causes the formation of different shapes during the process[73]. Another valid alternative is to use surfactant-free protocols. They consist of simple use of water as solvent that allow to develop straight-forward synthesis of single-phase selenium-based nanomaterials with a relatively high yield[74].

Some of the reducing agents that are being used in research are borohydrides, citrates, hydrazine and alcohols[74]. The reducing characters of the reactants influence the rate of reductions and, therefore, vary the experimental conditions and control the formation of the products.

Cobalt selenide. Cobalt selenides have remarkable properties, namely: electrical conductivity, abundance, structure, and outstanding electrochemical and electrocatalytic features. The CoSe has space group $P6_3/mmc$ and a crystal structure that consists of hexagonal planes of cobalt and selenium atoms[75]. The cubic $CoSe_2$ is considered one of the ideal catalysts in electrocatalytic water splitting application.

Nickel selenide. Nickel and selenium can give rise to a variety of nickel selenides, including stoichiometric and non-stoichiometric compounds. The valence electronic configuration of Ni ($3d^84s^2$) and small difference in electronegativity between Ni (x = 1.9) and Se (x = 2.4) are responsible for a variety of nickel selenide compounds[76]. There are three stable phases of nickel selenides at room temperature, including $NiSe_2$, NiSe, and Ni_3Se_2. The $Ni_{1-x}Se$ is a common formula observed of nickel selenides and in here the nickel content falls in-between 1.00 and 0.85. The atomic ratio between nickel and selenium in Ni_xSe_y influences the electronic structure and the electrocatalytic properties[76]. The nickel selenides with a non-stoichiometry such as $Ni_{0.85}Se$ have unsaturated atoms and it is of great interest exploring the electrocatalytic performance in water splitting. The bandgap of NiSe is about 2.0 eV[77]. Moreover, nickel selenides show different colors, for instance black color is observed for fine powders, while silver color is observed for larger crystals. In their crystal structure, selenides are in trigonal prismatic sites and nickels are in octahedral sites. Due to their interesting magnetic and electronic properties, nickel selenides arose the attention of researchers in the last 15 years, since their application in sensors, solar cells, water splitting and laser materials. The nickel selenides are excellent catalysts to replace precious Pt catalysts due to the abundant reserve, low cost, and good conductivity[78].

As mentioned before, great attention has been devoted to transition metal chalcogenides and dichalcogenides MX_2 (M = Fe, Mn, Ni, Co; X = Se, S, Te) due to their outstanding properties[74]. Their conductive behaviors range from semiconductor to metallic, and large-scale magnetic properties as well. The approach that allows to reach the production of such materials is selenization. Recently, selenization technologies have arose a lot of interest among researchers attention because of the possibility of developing low-cost materials[79].

Selenization processes involve the exposure of metallic precursors to a reactive selenium-based compound to produce the desired selenide compounds. A clear understanding of this kind of materials is of great importance for the optimization of growth parameters and the production of high-quality devices[79].

Recently, selenization of transition metal-based nanomaterials through chemical vapor deposition (CVD) process enabled the successful synthesis of TMCs and TMDs with high quality. Anyhow, the CVD approach requires annealing at high temperatures, ranging from 600°C to 1300°C. Furthermore, it is a time-consuming process, which severely limits the number of available substrates for the synthesis of such materials. Hence, the design of fast and low-cost protocols are a major challenge[80].

In this regard, surfactant-free methodologies that use water as a solvent have been developed for the synthesis of selenium-based nanostructures with relatively high yields (> 10 g) [81]. The protocols consist of simple mixing of aqueous precursor solutions followed by few hours thermal treatment which never exceed 100°C. Moreover, these kinds of methods do not require specific gaseous environments, but they can be easily led in air atmosphere at ambient pressure.

All of this meets the need of avoiding harsh conditions and faster synthesis methodologies, as it will be demonstrated throughout this thesis.

2. Outline of the thesis and objectives

The main aim is the investigation of the electrocatalytic properties of selenium-based materials for the development of new nano-systems for emerging applications such as water splitting. Selenium-based nanomaterials are the focus of this thesis, due to their value in technological applications and applications in scientific research. Since the properties of these materials depend on their composition and morphology, the main challenge is to fabricate nanomaterials with different compositions and novel morphologies.

In this context, I focused, from one hand, on the synthesis and the optimization of the electrocatalytic systems through rational designed surfactant-free synthesis protocols.

I propose a two-step facile synthesis method for the synthesis of selenium-based nanostructures. In the first step, nickel hexacyanoferrates (Ni-HCFs) and cobalt hexacyanoferrates (Co-HCFs) nanoparticles are obtained through a synthesis involving potassium ferricyanide ($K_3Fe(CN)_6$) and, according to the desired metal, Ni(II) and Co(II) precursor salts. In the second step, the selenization process is led using sodium hydroselenide (NaHSe), that allows to obtain selenium-based nanostructures for water splitting application.

On the other hand, I focused on the deep chemical and physical characterization as well. The development of ideal electrocatalytic systems, based on selenium without the need for more complex structures, is the other purpose of this thesis since the research of novel highly performant nanomaterials is desirable and challenging. Furthermore, the target is to reach low bandgap nanostructures able to produce hydrogen and oxygen efficiently.

Selenium has been chosen for its low cost compared to the state-of-the-art electrocatalysts based on noble metals and for its reported efficiency and stability in electrocatalytic reactions. Using sodium hydroselenide (NaHSe) as a selenium source on different nanomaterials, a new and innovative protocol able to produce low-cost and effective electrocatalysts has been developed. The effects of the selenization on the composition, morphology, structure, optical, and functional properties, are presented in this thesis.

3. Experimental section

3.1 Materials synthesis

3.1.1. Ni-HCF and selenization process

Materials. Nickel(II) acetate tetrahydrate $Ni(OCOCH_3)_2 \cdot 4H_2O$ (98%, Sigma-Aldrich), trisodium citrate dihydrate $HOC(COONa)(CH_2COONa)_2 \cdot 2H_2O$ (≥99.0%, Sigma-Aldrich), potassium ferricyanide $K_3Fe(CN)_6$ (≥99.0%, Sigma-Aldrich), sodium borohydride $NaBH_4$ (99%, Sigma-Aldrich), selenium Se (99.99%, Sigma-Aldrich), absolute ethanol (99%, Sigma-Aldrich) and deionized water (with conductivity < 20 μS/cm) were used for the preparation of the samples.

Synthesis. Ni-HCF nanocubes were prepared by a co-precipitation method according to works previously reported[82]. Briefly, 4.29 g of $Ni(OCOCH_3)_2 \cdot 4H_2O$ and 9.90 g of sodium citrate were dissolved in 600 mL of deionized water. In the meanwhile, 3.96 g of $K_3Fe(CN)_6$ were dissolved into 600 mL of deionized water. The above two solutions were then mixed at room temperature under continuous stirring for 48 hours. After the reaction was completed, a light-brown suspension was obtained. Finally, the precipitate was collected by centrifugation, washed with deionized water and ethanol several times, and then dried at 65°C overnight. Thus, 6.12 g of Ni-HCF nanocubes were obtained.
Then, the so-obtained nanocubes underwent to the second and last process: selenization using sodium hydroselenide (NaHSe). The selenization process was driven using NaHSe, previously synthesized by reducing selenium with sodium borohydride ($NaBH_4$). The obtained mild reducing agent was added dropwise to a Ni-HCF nanocubes aqueous solution. Briefly, 500 mg of Ni-HCF were dissolved through stirring in 100 mL of deionized water. The NaHSe solution was obtained dissolving 237 mg of selenium powder and 227 mg of $NaBH_4$ in 50 mL of deionized water according to the reaction:

$$4NaBH_4 + 2Se + 7H_2O \rightarrow 2NaHSe + Na_2B_4O_7 + 14H_2 (\uparrow)$$

After the addition of the NaHSe solution, the reaction process was kept at 100°C for 3 hours. The black precipitates were centrifuged, rinsed with deionized water and ethanol, and finally dried in an oven at 65°C overnight.

3.1.2. Co-HCF and selenization process

Materials. Cobalt(II) nitrate hexahydrate $Co(NO_3)_2 \cdot 6H_2O$ (98%, Sigma-Aldrich), potassium ferricyanide $K_3Fe(CN)_6$ (≥99.0%, Sigma-Aldrich), sodium borohydride $NaBH_4$ (99%, Sigma-Aldrich), selenium Se (99.99%, Sigma-Aldrich), absolute ethanol (99%, Sigma-Aldrich) and deionized water (with conductivity < 20 μS/cm) were used for the preparation of the samples.

Synthesis. Cobalt hexacyanoferrate (Co-HCF) nanocubes were synthesized according to the following process. Firstly, 0.1 g of $K_3Fe(CN)_6$ were dissolved in 50 mL of deionized water. Secondly, 1 mmol of $Co(NO_3)_2$ was added dropwise under vigorous stirring to the above solution. The reaction was kept at room temperature for 12 hours. After the completion of the reaction, a ruby-red solution was obtained. The resulting precipitates were filtered, washed with deionized water and ethanol, and finally dried in an oven at 65°C overnight. Thus, 424 mg of Co-HCF nanocubes were obtained.

As in the previously reported material, Co-HCF nanocubes were involved in a selenization process using NaHSe. The mild reducing agent was added to a Co-HCF aqueous solution. In this synthesis, 200 mg of Co-HCF were dissolved in 100 mL of deionized water and then 50 mL of a 60 mM NaHSe fresh solution were added dropwise (according to the process described above).
After that, the reaction process was kept at 100°C for 2 hours. The dark grey precipitates were centrifuged, rinsed with deionized water and ethanol, and finally dried in an oven at 65°C overnight.

3.2 Materials characterization

The crystallographic structure of the as-prepared samples was determined by X-ray diffraction patterns collected using an X-ray diffractometer (PanAnalytical Empyrean XRD) with Cu Kα radiation in the range 2θ between 10° and 80°. The elemental analysis and the morphologies of the samples were determined through SEM images and corresponding elemental mappings obtained by a field-emission scanning electron microscopy (FESEM), Magellan XHR 400L with a 5 kV electron beam equipped with an energy dispersive X-ray spectrometer (EDS). FTIR spectra of Ni-HCF and Co-HCF were collected using Vertex 80v vacuum-based FTIR spectrometer from Bruker equipped with a Platinum Diamond attenuated total reflectance (ATR). UV-Visible absorption and reflectance spectra were collected with a Agilent Cary 5000 spectrophotometer between 800 and 200 nm.

3.3 Electrochemical measurements

The performances of the as-synthesized catalysts towards oxygen evolution reaction were tested in a three-electrode configuration system at room temperature on an electrochemical workstation (Solartron Analytical, ModulabXM). Glassy carbon electrodes (GCE) with a diameter of 3.0 mm, Ag/AgCl (3 M KCl), and graphite were used as working, reference, and counter electrodes, respectively. Linear sweep voltammetry (LSV) was performed in 1.0 M KOH electrolyte in the range of potential starting from -0.05 V to 0.9 V (vs RHE) with a scan rate of 5 mV/s. Cyclic voltammetry (CV) was conducted in non-faradic region (from -0.05 to 0.25 V vs RHE) in 1.0 M KOH electrolyte with different scan rates (40, 60, 80, 100, 120, 140, 160, 180, 200 mV/s). The potential of the reference electrode was converted to a reversible hydrogen electrode (RHE) by the formula:

$$E_{(RHE)} = E_{(Ag/Ag\,Cl)} + 0.059*pH + 0.1976$$

with 14.0 pH. The catalyst was prepared by dispersing 5 mg of each powder in 20 μL Nafion (5 wt. % in lower aliphatic alcohols and water, contains 15-20% water, Sigma-Aldrich) and 200 μL isopropyl alcohol (99.5%, Sigma-Aldrich) solution by stirring for 1 hour. Then, the working electrode was prepared by dropping 5 μL of each catalyst ink on the GCE. The mass loading of active materials on the working electrode was about 0.295 mg cm^{-2}. Electrochemical impedance spectroscopy (EIS) was measured at different overpotential (vs RHE) over the frequency range from 100 kHz to 10 mHz at Ac amplitude of 10 mV.

4. Results and discussion

4.1 Ni-HCF and Ni-HCF selenized

4.1.1 UV-Visible

The optical properties of the synthesized samples have been measured through a UV-Visible spectrophotometer in reflectance mode. In **Figure 4** and **5** optical resistance spectra for Ni-HCF and Ni-HCF selenized samples under investigation are reported.

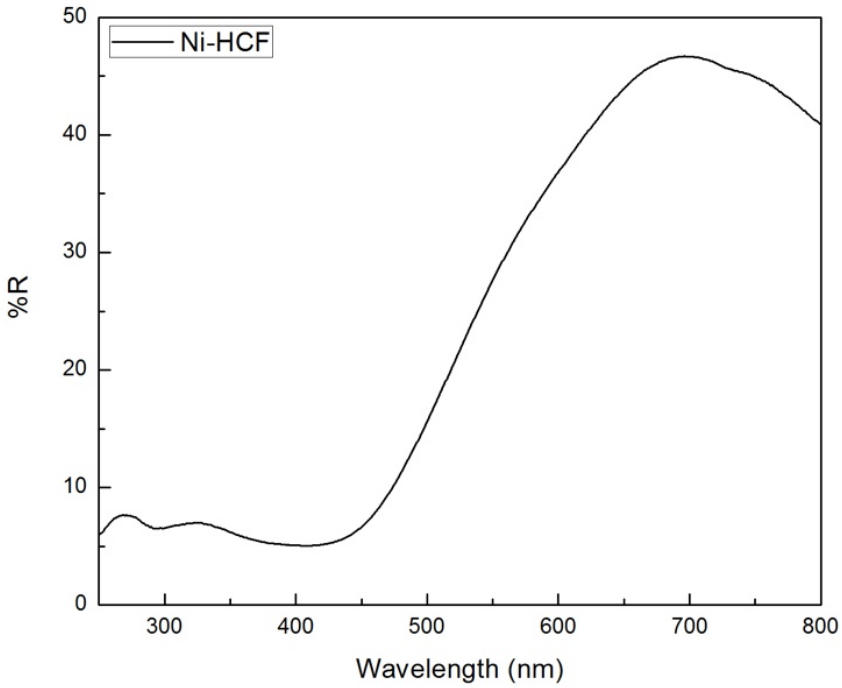

Figure 4. Optical reflectance spectrum of Ni-HCF sample.

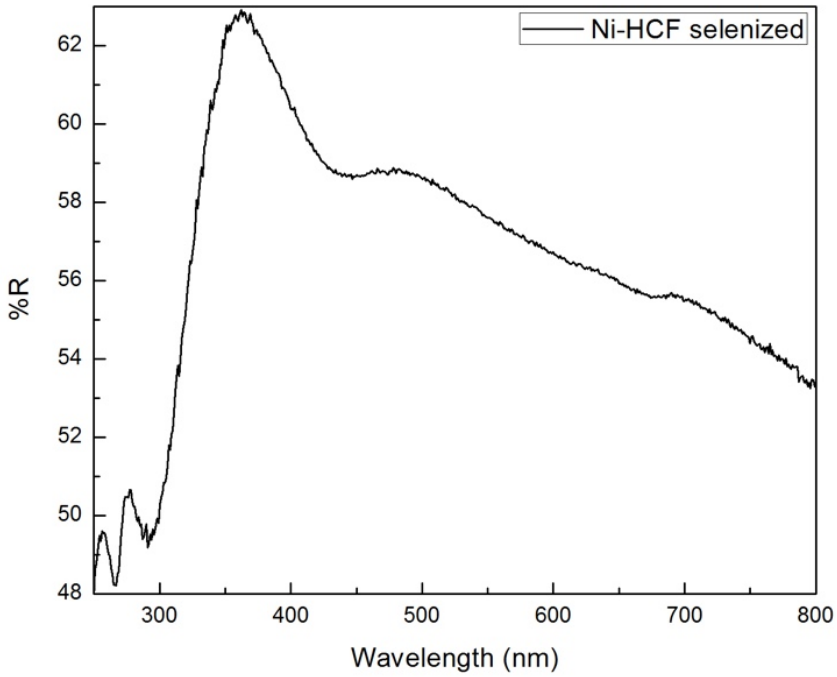

Figure 5. Optical reflectance spectrum of Ni-HCF selenized sample.

From reflectance spectra in **Figure 4** and **5** respectively, it is worth noting that there is a change in the position of the absorption peaks. According to this optical result, the selenization process appears to shift the absorption towards smaller wavelengths, moving the maximum of reflectance from 700 nm to 350 nm.

Since optical properties and the ability to generate electron-hole pairs depend on the bandgap of the materials, this parameter must be determined through UV-Vis characterization.

When an electromagnetic irradiates the surface of solid powder, diffuse reflection (DR) may occur. The diffuse reflection (DR) is the radiation that penetrates the powder sample and undergoes scattering and wavelength-dependent absorption within the nanomaterial. Some part of this radiation leaves the bulk sample in all directions. In this case, a DR accessory is designed to collect the diffused reflection and directs it into a photodetector. The accessory has a spherical surface and it is known as an integrating sphere and it is coated with a white standard reflecting thin film.

The measurement of diffuse reflection (DR) with a UV-Vis spectrophotometer is a standard method to determine the optical properties of powder nanomaterials. In the case of semiconducting powder nanomaterials, these properties are the absorption coefficient (K) and bandgap energy (E_g). E_g is an important feature for semiconducting nanomaterials since it determines the feasibility of optoelectronic

applications. Powder samples are filled into a cylindrical sample holder with a surface of 1 cm^2. The powders should form a few mm thick layer for the incident light to be absorbed or scattered before reaching the back surface of the sample.

Kubelka and Munk proposed the idea of calculating the E_g through DR spectra[83]. Their equation can be written as follows:

$$\frac{K}{S} = \frac{(1 - R_\infty)^2}{2R_\infty} \equiv F(R_\infty)$$

Where K is the molar absorption coefficient, S is the scattering coefficient, R_∞ is the diffuse reflectance and $F(R_\infty)$ is the Kubelka-Munk function. The bandgap and absorption coefficient are related through the well-known Tauc relation[84]. The Tauc relation for an indirect bandgap material is given by the expression:

$$\alpha h\upsilon = A\,(h\upsilon - E_g)^n$$

Where α is linear absorption coefficient, υ is the frequency of the light and A is the proportionality constant. The "n" parameter is taken to be 1/2 for indirect bandgap materials. When the incident radiation scatters diffusely, the absorption coefficient K becomes equal to 2α. If we consider the scattering coefficient as a constant with respect to the wavelength, the Kubelka-Munk function is proportional to the α and applying it we obtain:

$$[F(R_\infty)h\upsilon]^2 = A\,(h\upsilon - E_g)$$

Plotting $[F(R_\infty)h\upsilon]^2$ vs the energy (in eV), the value of the bandgap of the sample can be easily found fitting a straight line for the straight portion of the curve. By extrapolating the tangent to the axis of abscissa, the exact value of the bandgap is given.

For the case of Ni-HCF nanomaterials, in literature, it is reported a value of 1.4 eV for the bandgap[85]. The Tauc plots of the Ni-HCF and Ni-HCF selenized nanocubes are presented in **Figures 6** and **7**.

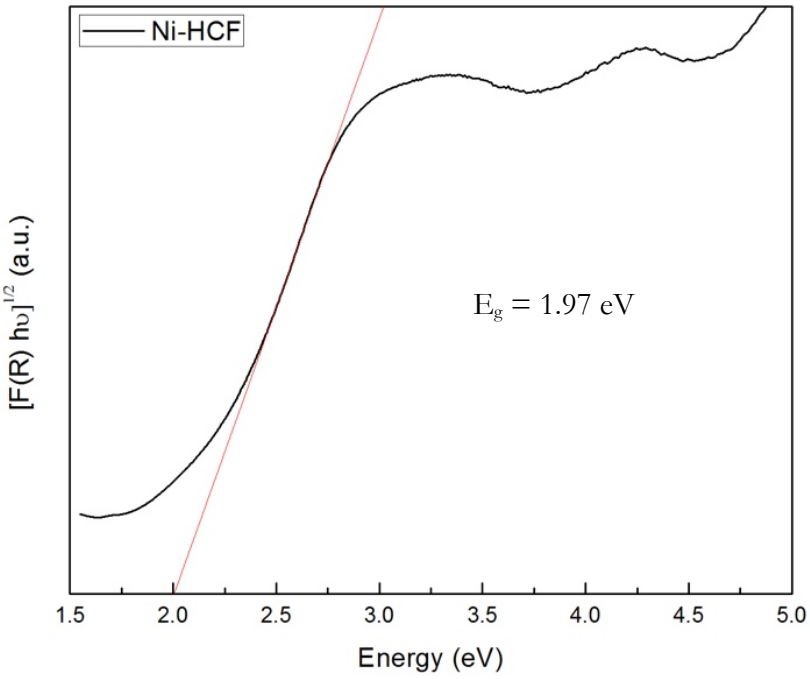

Figure 6. Tauc plot of Ni-HCF sample.

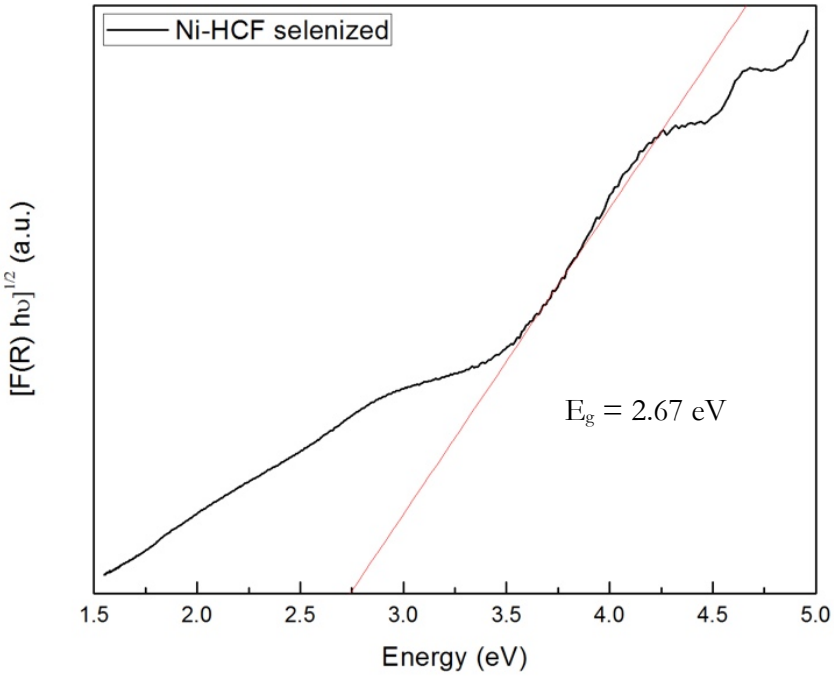

Figure 7. Tauc plot of Ni-HCF selenized sample.

It can be observed that the profile of the selenized sample has been shifted towards higher energies compared to the pure Ni-HCF sample. This means that the band gap has been broadened due to the introduction of selenium atoms in the structure. The Ni-HCF sample shows a bandgap of 1.97 eV, while the selenized sample shows a bandgap of 2.67 eV. A comparison between experimental values obtained through this method and the values reported in the literature is reported in **Table 1**:

E_g Ni-HCF (literature)	**E_g Ni-HCF**	**E_g Ni-HCF selenized**
1.40 eV [85]	1.97 eV	2.67 eV

Table 1. Comparison of the bandgap values obtained experimentally and from literature for Ni-HCF-based samples.

These results confirm that the selenization process driven on the Ni-HCF broadened the bandgap of the sample due to the insertion of selenium elements in the nanostructure, affecting its ability to harvest light compared to literature's band gaps.

4.1.2 X-ray Diffraction Analysis

The crystallographic structure of Ni-HCF and Ni-HCF selenized samples has been determined using an X-ray diffractometer (PanAnalytical Empyrean XRD) with Cu Kα radiation in the range 2θ between 10° and 80°. The patterns of these two samples are shown in **Figure 8**.

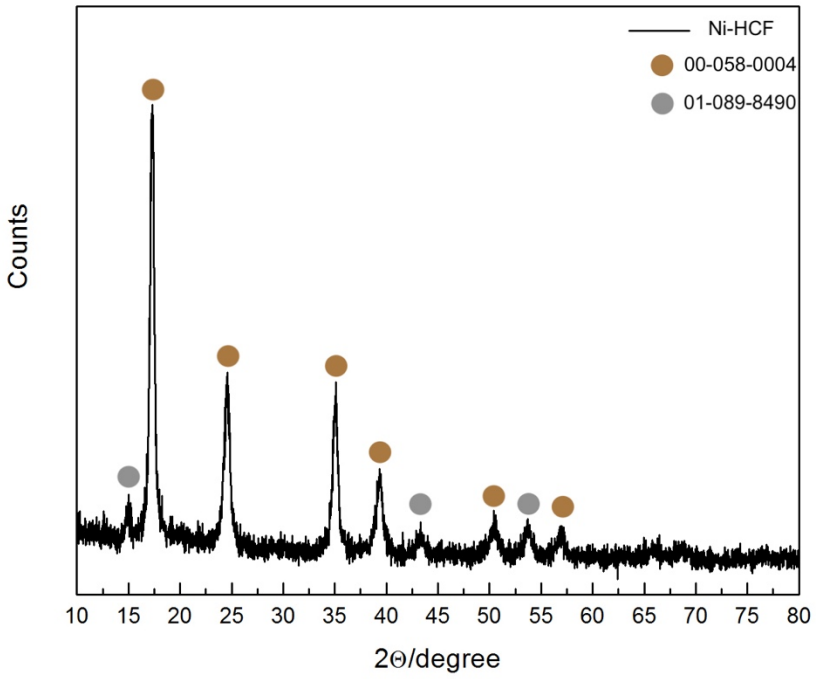

Figure 8. XRD pattern of Ni-HCF sample.

The Ni-HCF sample shows six main peaks at a value 2θ of: 17.4°, 24.6°, 35.3°, 39.5°, 50.4°, and 57.2°. These peaks have been assigned to the iron-nickel cyanide phase (reference code: 00-058-0004, in brown). The peaks correspond to the (200), (220), (400), (420), (440), and (620) peaks of the iron-nickel cyanide phase, respectively. Some weaker peaks at 2θ value of 14.8°, 43.4°, 53.9°, and 57° have been observed as well. The presence of these peaks can be justified by the presence of a carbon phase (reference code: 01-089-8490, in grey). According to the XRD pattern, it can be confirmed that the Ni-HCF nanocubes show an overall crystalline phase, since it is normal to have carbon peaks for this kind of synthetic routes coming from unreacted precursors.

Concerning the Ni-HCF sample that have been selenized, its XRD pattern is reported below (**Figure 9**).

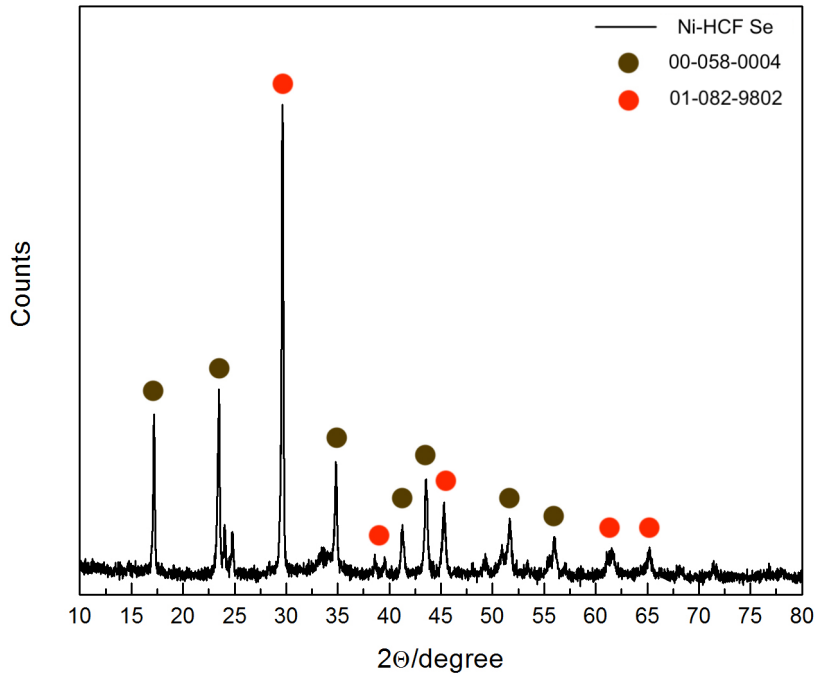

Figure 9. XRD pattern of Ni-HCF selenized sample.

As in the previous case, the Ni-HCF sample that has been selenized shows the six characteristic peaks of iron-nickel cyanide phase (reference code: 00-058-0004, in dark-brown) at 2θ values of: 17.4°, 24.6°, 35.3°, 39.5°, 50.4° and 57.2°. The presence of iron selenide (reference code: 00-082-9802, in red) has been detected due to the appearance of five peaks at 29.7°, 38.6°, 45.2°, 62.6° and 65.2° corresponding to (101), (111), (022), (202) and (203) iron selenide peaks, respectively. These results suggest that the Ni-HCF inner core has been preserved during the selenization process, while on the outer shell there was the formation of iron selenide. This means that the selenization of the Ni-HCF nanostructures brought to the generation of core-shell structures, where the Ni-HCF is the inner core and the iron selenide is the outer shell. According to the elemental mapping, EDS analysis could confirm the presence of this kind of composite nanostructure.

The presence of a signal coming from iron selenide confirms that the selenization process has been driven properly with a correct integration of selenium in the crystal structure of the Ni-HCF nanocubes.

4.1.3. Scanning Electron Microscopy

The morphology of as prepared nanocubes was examined through field-emission scanning electron microscope (FESEM) and representative images of Ni-HCF and Ni-HCF selenized are shown in **Figure 10** and **11,** respectively.

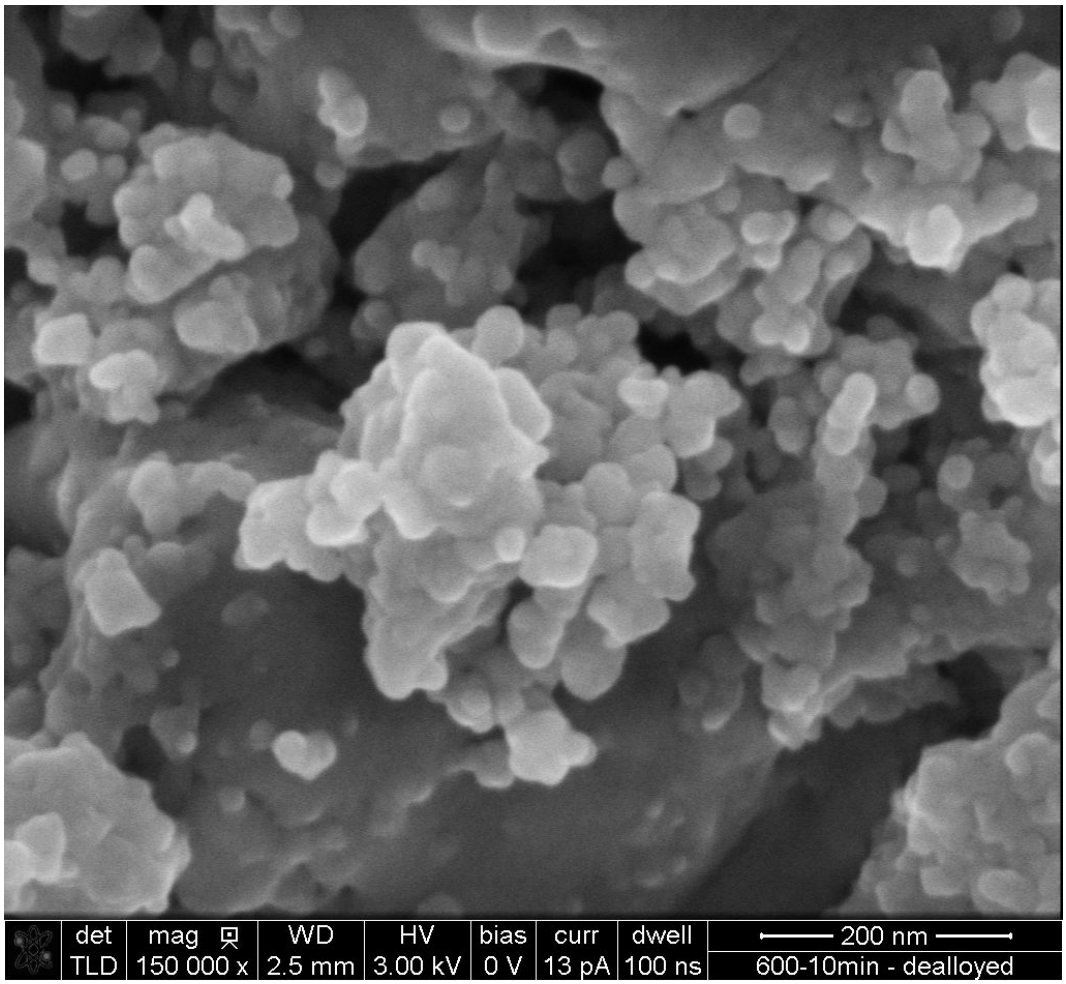

Figure 10. Morphology of Ni-HCF sample.

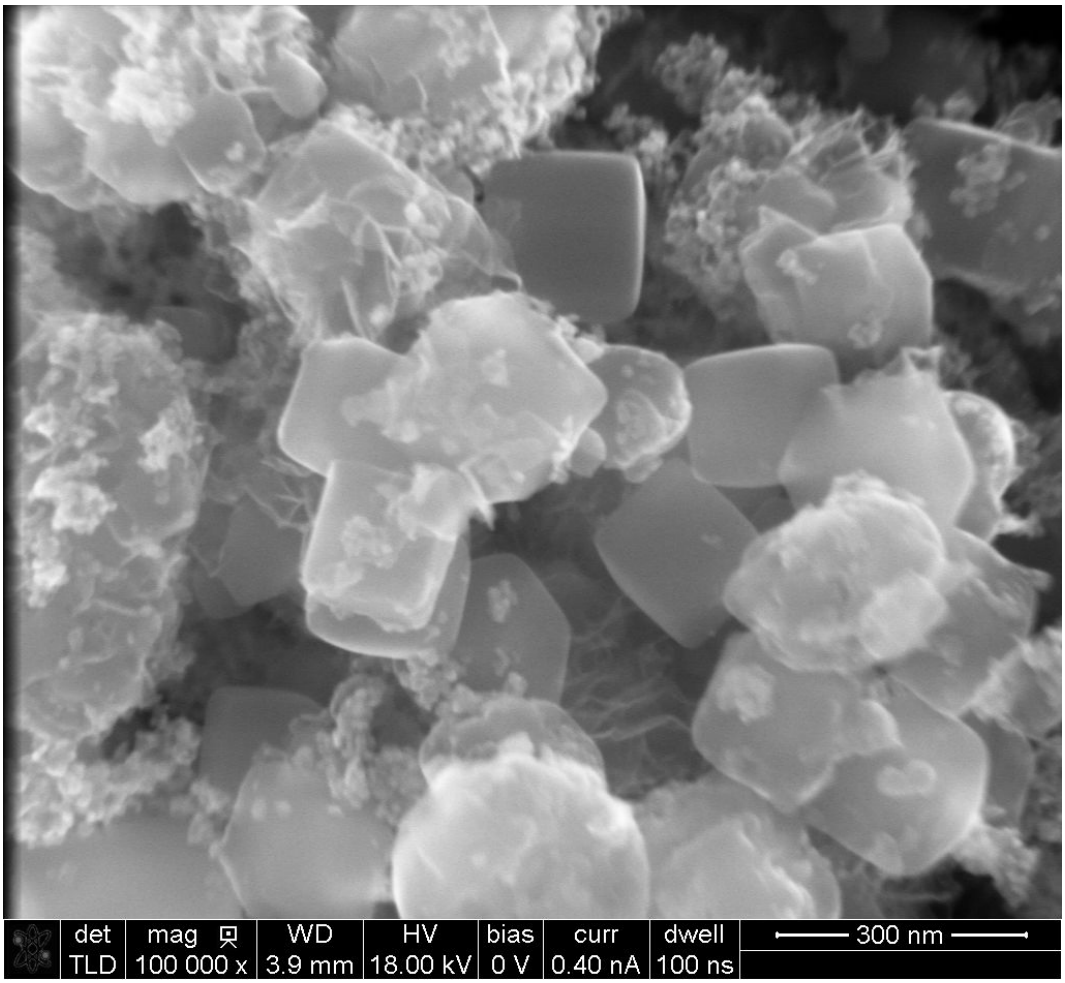

Figure 11. Morphology of Ni-HCF selenized sample.

Not in both cases the presence of nanocubes was observed. The non-selenized sample reveals the presence of random nanoparticles with an average dimension of 50 nm forming non-homogeneous aggregates. The failure in the synthesis of cubic nanostructures is attributable to a non-homogeneous stirring in the synthesis process that favored the aggregation of the nanoparticles and impaired the growth of the nanocubes.

On the other hand, using the previous mentioned Ni-HCF sample and leading a selenization process on it using NaHSe, the formation of nanocubes was achieved. Nanocubes ranging from 223 nm to 629 nm in dimension were obtained, suggesting a strong contribution of NaHSe to the growth of such nanostructures. The same sample without any treatment was showing random nanoparticles, while the use of a mild reducing agent and of a thermal treatment at 100°C for 3 hours seem to enhance the formation of cubic structures with well-defined edges and shapes.

4.1.4 Energy Dispersive X-ray Spectroscopy

The field-emission scanning electron microscopy was equipped with an energy dispersive X-ray spectrometer (EDS), allowing to perform the elemental mapping. The following micrographs (**Figures 12**, **13** and **14**) for the Ni-HCF nanostructures that have been selenized were obtained.

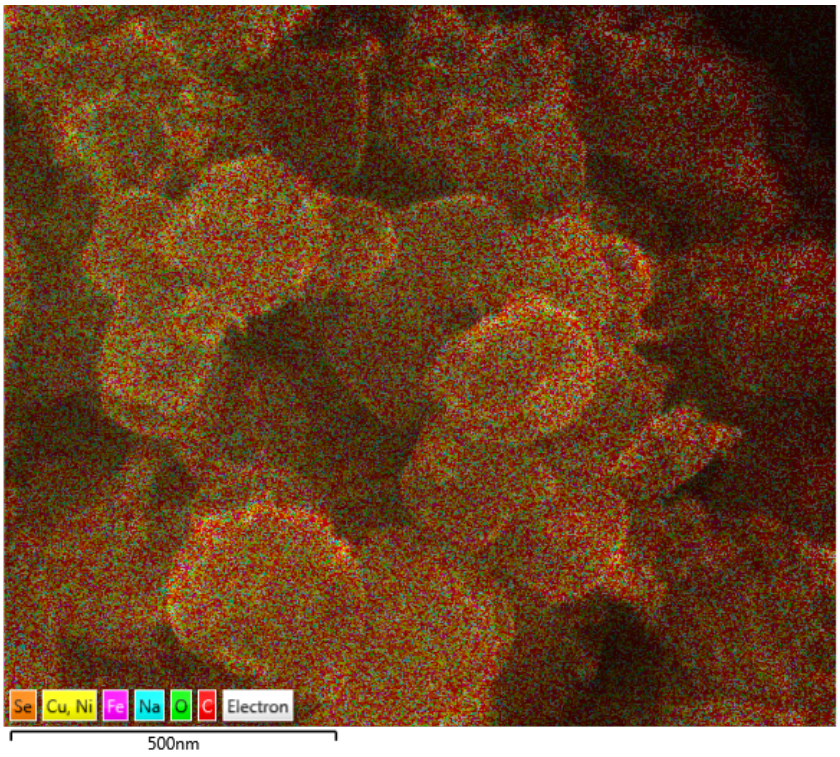

Figure 12. Elemental mapping of Ni-HCF selenized sample.

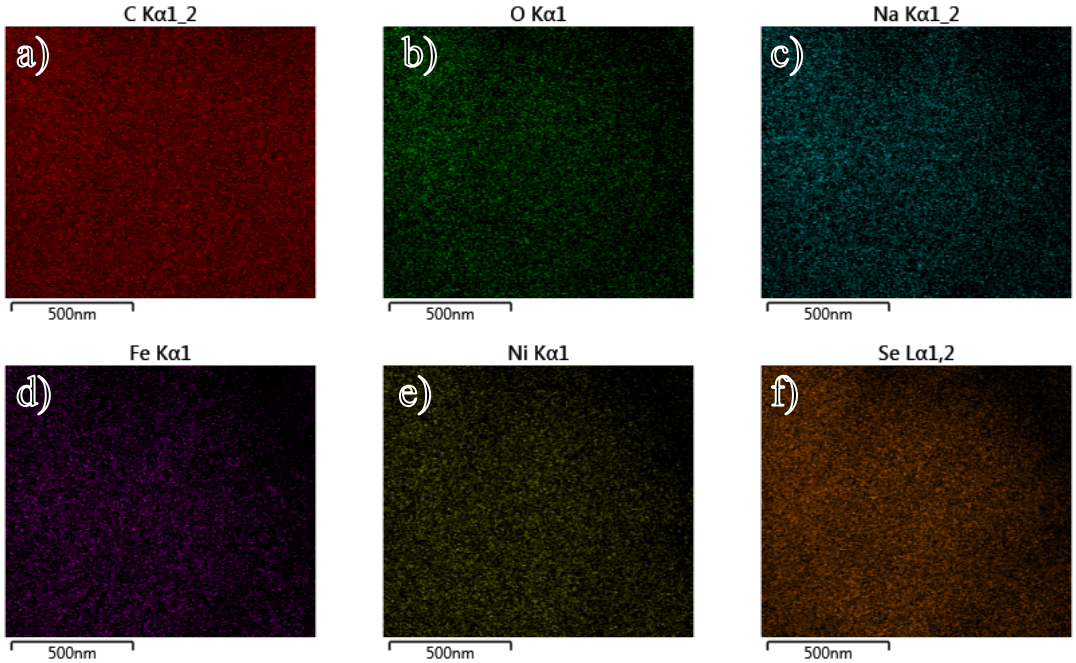

Figure 13. Elemental mapping of (a) carbon, (b) oxygen, (c) sodium, (d) iron, (e) nickel and (f) selenium of Ni-HCF selenized sample.

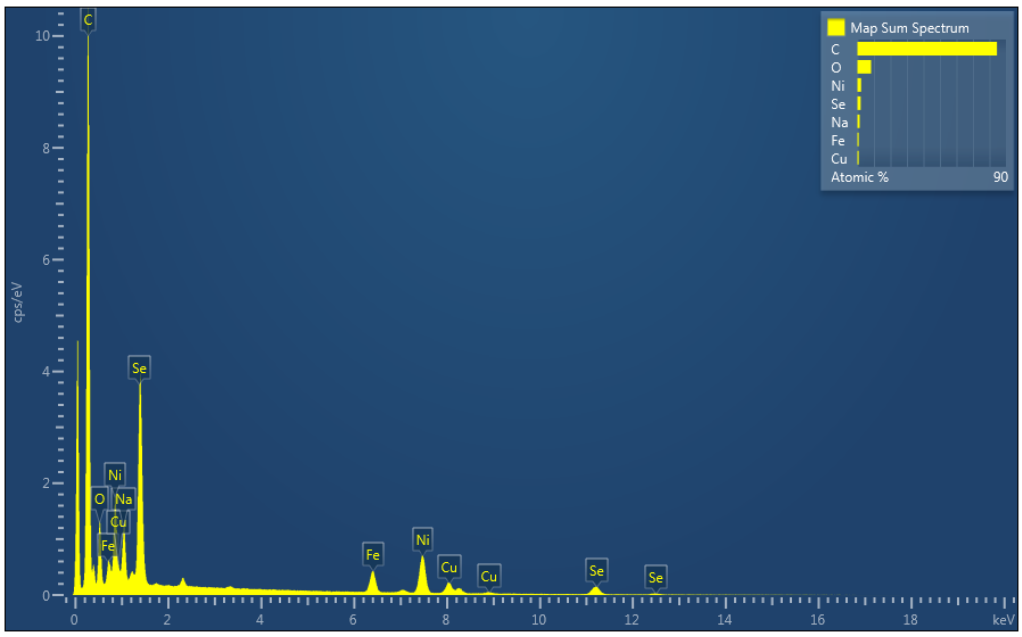

Figure 14. EDS graph of Ni-HCF selenized sample.

From the EDS analysis, the presence of carbon, oxygen, sodium, iron, nickel, copper, and selenium was detected, as confirmed by the EDS mapping in **Figure 14** as well. The signal coming from copper is related to the tape that was used for the immobilization of the powder on the support (stabber). On the contrary, the signals coming from oxygen and sodium are related to the precursors that were used for the synthesis of these materials. This result could suggest imperfect washing process after the centrifugation since ethanol and water should eliminate the presence of such impurities.

As an alternative to explain the presence of oxygen, also the following hypothesis are valid: (i) adsorbed oxygen molecules at the surface; (ii) partial surface oxidation of the selenide compound at the surface; (iii) a malfunctioning of the pre-vacuum chamber of the microscope. Also these factors can be considered to justify the presence of a signal coming from oxygen.

On the other hand, **Figure 14** makes it possible to observe the presence of both iron and selenium at the surface. This confirms that core-shell structures with Ni-HCF cores and iron selenide shells were obtained, reinforcing the observations that were previously done analyzing the XRD patterns.

So it can be claimed that the selenization process affects the surface, the morphology and the structure of the nanomaterial.

4.1.5 Fourier-Transform Infrared Spectroscopy

Infrared (IR) spectrum was collected using a Vertex 80v. The IR spectrum related to the Ni-HCF sample, taken as an example, is reported below (**Figure 15**).

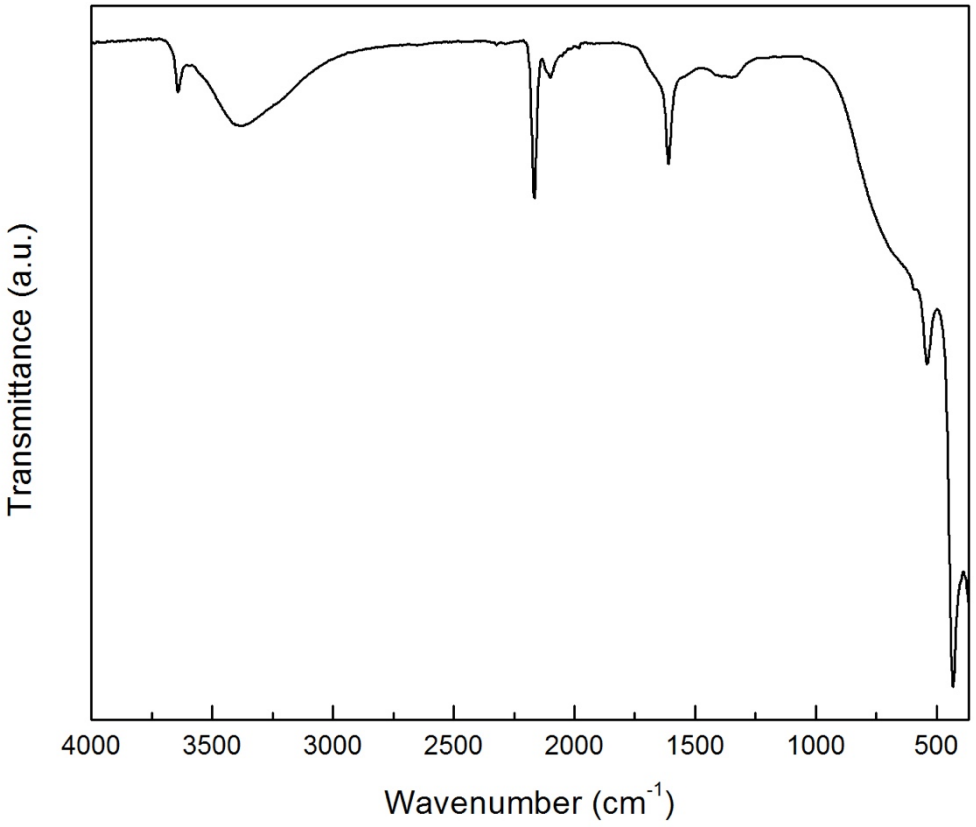

Figure 15. FTIR spectrum of Ni-HCF sample.

Ni-HCF spectrum is characterized by the presence of two major absorption peaks due to the presence of CN groups and water molecules. The absorption band over the range of 2900-3750 cm^{-1} indicates the presence of -OH groups. The presence of a sharp peak at 3642 cm^{-1} is attributable to strongly hydrogen-bonded water molecules in the structure, as reported in the literature[86]. The sharp peak at 2167 cm^{-1}, instead, corresponds to Fe^{III}-CN-Ni^{II} linkages. Another less intense peak noticed at 2084 cm^{-1} arises probably due to unreacted potassium ferricyanide, while in the range between 434 cm^{-1} and 544 cm^{-1} the presence of Ni-C stretching and Ni-CN bending is observed.

Unfortunately, no IR spectra of the Ni-HCF selenized sample could have been acquired to determine the effect of the selenization on the structure.

4.1.6 Electrochemical measurements

The electrochemical properties of Ni-HCF and Ni-HCF selenized nanocubes were further investigated as electrode materials for oxygen evolution reaction by using a three-electrode cell.

To evaluate the OER activity of the as-prepared catalysts, the Ni-based materials were loaded onto glassy carbon (GC) electrodes and were investigated using electrochemical linear sweep voltammetry (LSV), electrochemical impedance spectroscopy (EIS) and cyclic voltammetry (CV) technique in 1 M KOH (pH 14) electrolyte.

The electrocatalytic performance of the as-fabricated Ni-HCF and Ni-HCF selenized for OER was firstly evaluated by the LSV. **Figure 16** shows the LSV curves of Ni-HCF and Ni-HCF selenized electrocatalysts.

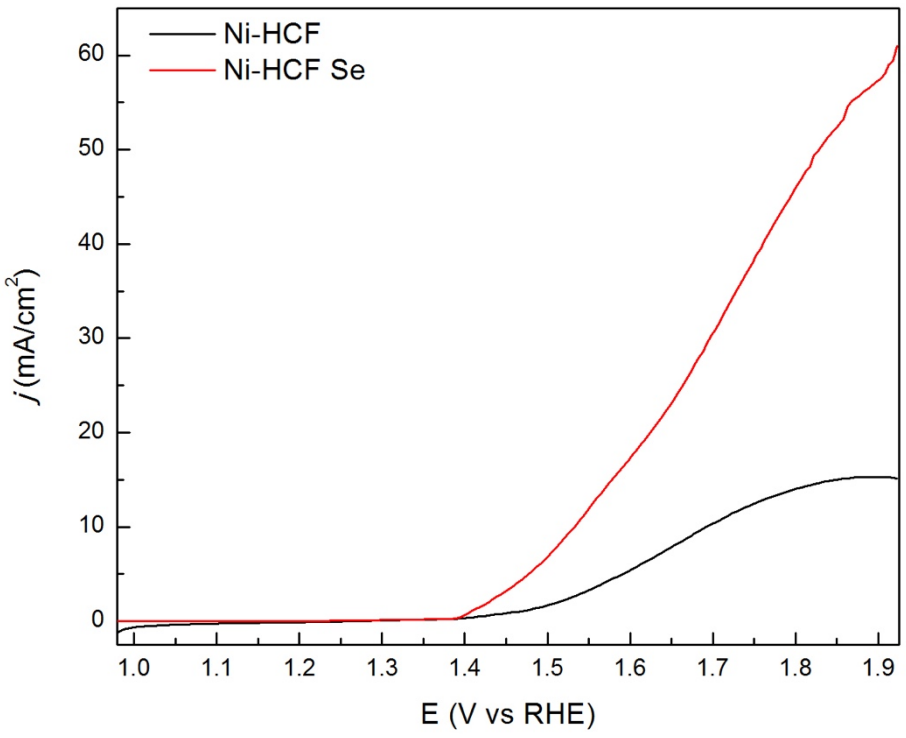

Figure 16. Linear sweep voltammetry measurement led on Ni-HCF and Ni-HCF selenized samples.

The Ni-HCF electrocatalyst exhibits greatly enhanced electrocatalytic performance compared to bare Ni-HCF. The current density of 10 mA cm^{-2} is the operation current of solar fuel synthesis, the working voltage under this value is important to evaluate the performance for OER electrocatalyst. The sample that has been selenized exhibits the lowest overpotential of 300 mV (vs RHE) at a current density of 10 mA/cm^2, which is much lower than the non-selenized sample (460 mV vs RHE) and similar compounds

reported in literature (425 mV vs RHE). In addition, the selenized electrocatalyst exhibits the smallest onset overpotential, that is 160 mV (vs RHE), compared to bare Ni-HCF (180 mV vs RHE) and other Ni-HCF-based nanomaterials (280 mV vs RHE), as shown in **Table 2**.

Material	Overpotential (mV) to reach 10 mA/cm^2	Reference
Ni-HCF selenized	300	-
Ni-HCF	460	-
NiHCF/MWCNTs	360	[87]
NiHCF/ITO	364	[88]
NiFeO NCs	320	[89]

Table 2. Comparative list of experimental data and literature reported ones.

It must be highlighted that the onset potential value for the Ni-HCF selenized sample is lower than those of conventional noble metal-based electrodes for OER. Moreover, the current density of the selenized sample reaches 57 mA/cm^2 at 1.9 V (vs RHE), which is 3.8 times higher than that of bare Ni-HCF nanostructures.

As mentioned before, the Tafel slope is an important parameter for evaluating OER catalytic kinetics. To further analyze the electrocatalytic activity of as-obtained electrocatalysts for OER, Tafel plots of the Ni-HCF and Ni-HCF selenized nanocubes were derived from LSV curves by fitting the linear regions according to the Tafel equation. The corresponding results are shown in **Figure 17** and **18**.

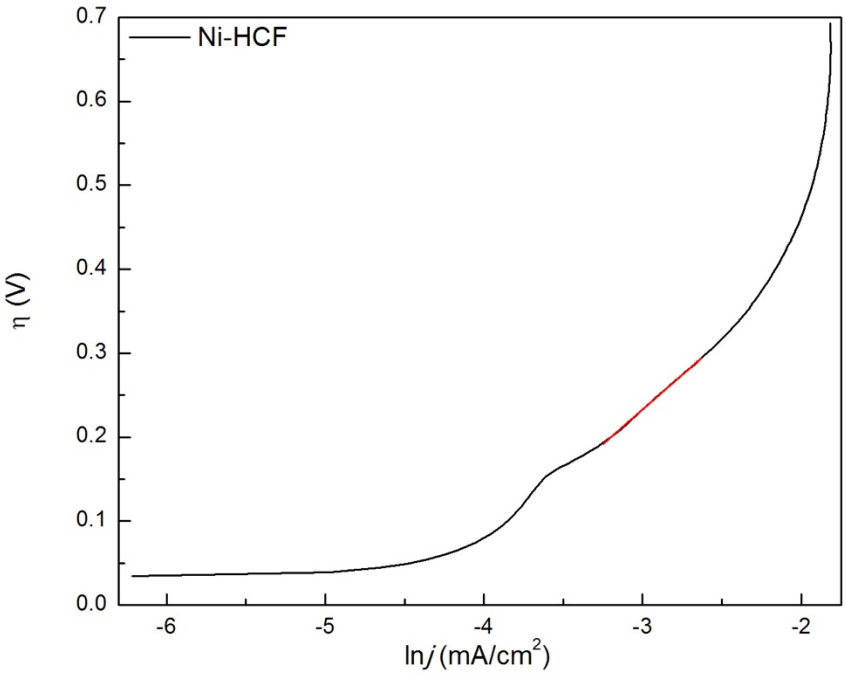

Figure 17. Tafel slope plot for Ni-HCF sample.

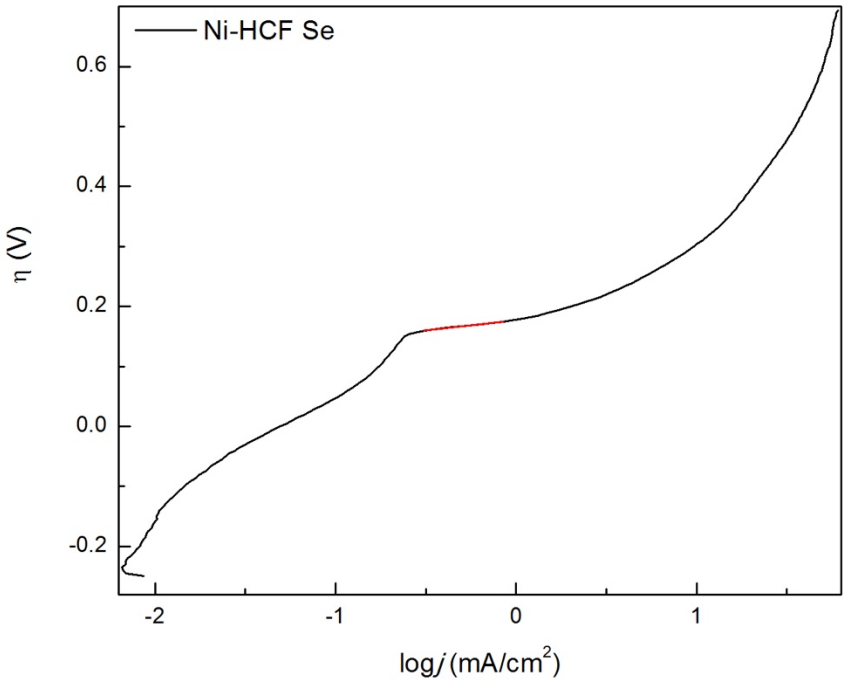

Figure 18. Tafel slope plot for Ni-HCF sample.

It can be observed that the selenized Ni-HCF catalyst shows a Tafel slope of 33 mV dec^{-1}, lower than that of bare Ni-HCF (165 mV dec^{-1}). It is well-known that the smaller is the value of the Tafel slope, the

lower overpotential will be required for electrocatalyst to achieve higher current density in the process of OER electrocatalysis. This indicates that the selenized sample possesses a higher electrocatalytic reactivity towards OER and suggests a faster charge transfer. The reason for this result can be attributed to the coupling of both Ni-HCF and elemental selenium, whose d-orbitals ensure an electron-rich molecular configuration. Based on these results (listed in **Table 3**), it is shown that the selenization process driven on the Ni-HCF catalyst brought to outstanding performance for water oxidation compared to the bare Ni-HCF.

Material	Onset potential @0.5 mA/cm² (mV)	Reported onset potential (mV)	Tafel slope (mV/dec)	Reported Tafel slope (mV/dec)
Ni-HCF	180	280	165	44 [88]
Ni-HCF selenized	160	-	33	-

Table 3. Comparison of the catalytic performances between Ni-HCF electrocatalyst for OER.

To further understand the role of selenization in enhancing the OER electrocatalytic performance compared to bare Ni-HCF nanoparticles, the electrochemically active surface areas (ECSA) of bare Ni-HCF nanostructures and selenized Ni-HCF electrocatalyst were estimated by the electrochemical double-layer capacitance (C_{dl}) acquired through CV tests at the different scan rates (**Figure 19, 20** and **21**).

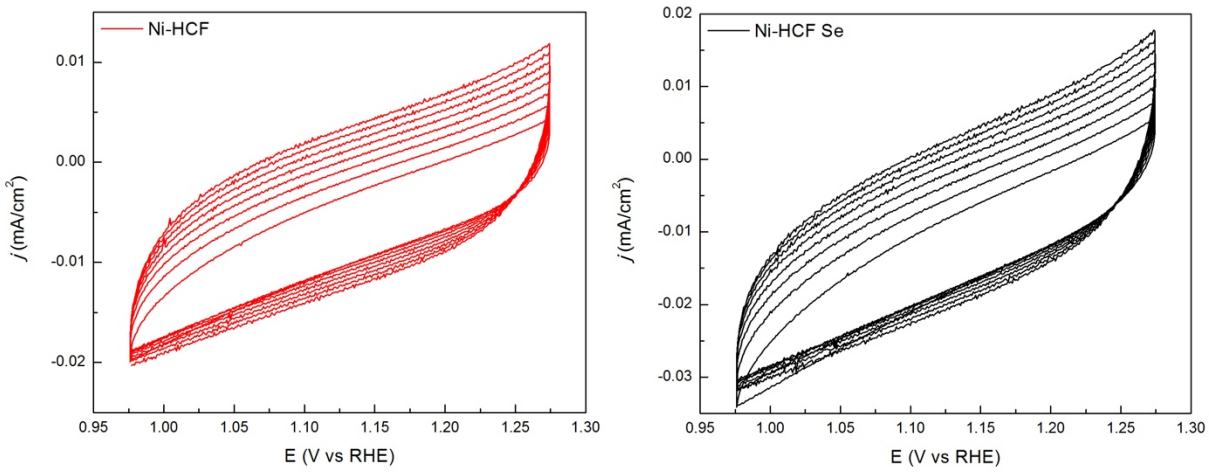

Figure 19 and 20. CV curves of Ni-HCF (left) and Ni-HCF selenized (right) catalysts at different scan rates.

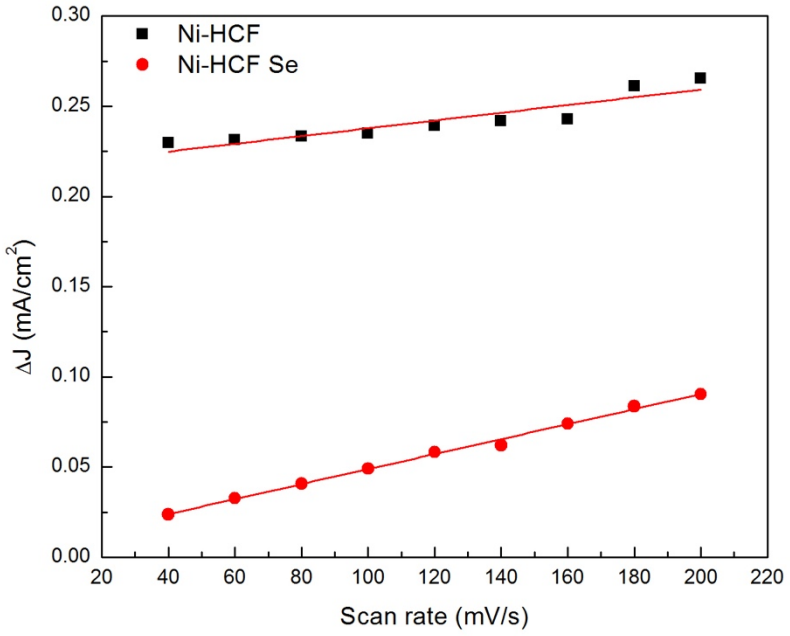

Figure 21. Linear plots of double-layer current as a function of the scan rate for Ni-HCF (black) and Ni-HCF selenized (red).

As can be seen from **Figure 19** and **20**, it is observed that the current density of selenized Ni-HCF electrocatalyst is slightly higher than that of bare Ni-HCF electrocatalyst. Instead, as seen in **Figure 21**, the C_{dl} value of as-fabricated Ni-HCF (2.16 mF cm^{-2}) is about 5.1 times higher than selenized Ni-HCF nanoparticles (0.42 mF cm^{-2}), demonstrating that the bare sample possesses higher ECSA and more active sites, even if the selenized samples has a lower onset potential.

Furthermore, to further understand the OER activity, electrochemical impedance spectroscopy (EIS) of Ni-HCF and Ni-HCF selenized was tested at a constant potential of 550 mV (vs. RHE). The Nyquist plots of bare Ni-HCF (**Figure 22**) and Ni-HCF selenized (**Figure 23**) are presented below.

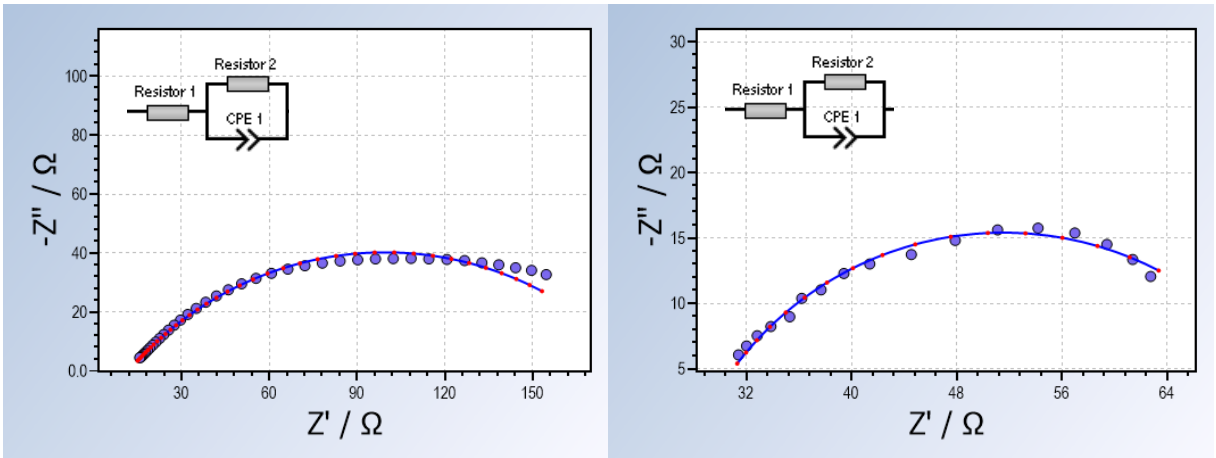

Figure 22 (left) and 23 (right). Nyquist plots of Ni-HCF (left) and Ni-HCF selenized (right) in 1.0 M KOH electrolyte at the potential of 550 mV.

From a geometrical point of view, the Nyquist plots of the sample catalysts consist of a semicircle that reveals the charge transfer resistance (R_{ct}) at the interface of electrode/electrolyte. The insets represent the equivalent circuits used to obtain the charge transfer resistance of the OER catalysts. In general, the high frequency resistance is mainly related to the solution resistance that is an ohmic resistance. The parameters to calculate the capacitance were obtained using RelaxIS 3 software fitting the equivalent circuit in order to give an interpretation of the kinetics. The corresponding values are listed in **Table 4**.

Material	Resistance 1 (Ω)	Resistance 2 (Ω)	CPE (S-sec$^{0.5}$)	α (0 < α < 1)
Ni-HCF	11.83	175.5	0.00014	0.548
Ni-HCF selenized	28.16	46.79	0.0083	0.742

Table 4. Simulated values of resistance (R_1 and R_2), capacitance (CPE) and α of EIS spectra calculated by equivalent circuit through RelaxIS 3 software.

Where "Resistance 1" and "Resistance 2" are related to the equivalent circuit used for the fitting, CPE is the capacitance and α.

The capacitance values have been calculated as:

$$C = (Q(R_1)^{(1-\alpha)})^{\frac{1}{\alpha}}$$

Where R_1 is the solution resistance, Q is a fitting parameter of the CPE and α is the fitting exponent factor, which varies from 0 to 1. When this last parameter approaches 0, the CPE behaves as a pure resistor, while when it approaches 1, it represents a pure capacitor. According to these parameters, the

selenized sample shows a quasi-capacitor behavior, opening up to new possible applications such as supercapacitors in addition to the good OER catalytic features.

4.2 Co-HCF and Co-HCF selenized

4.2.1 UV-Visible

As for the previous samples, the optical properties have been measured through a UV-Visible spectrophotometer. **Figure 24** and **25** present the optical resistance spectra for Co-HCF and Co-HCF selenized samples.

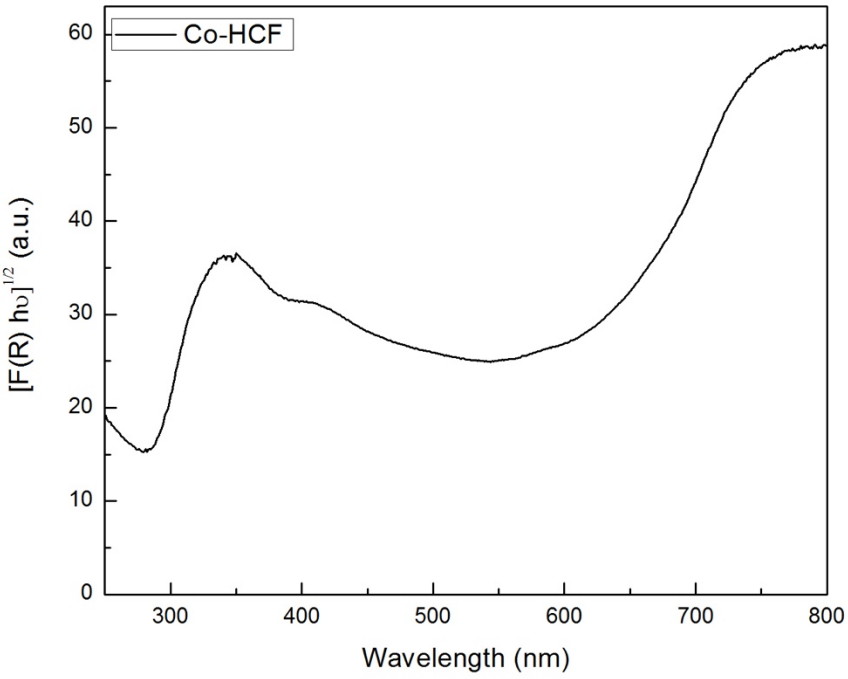

Figure 24. Optical reflectance spectrum of Co-HCF sample.

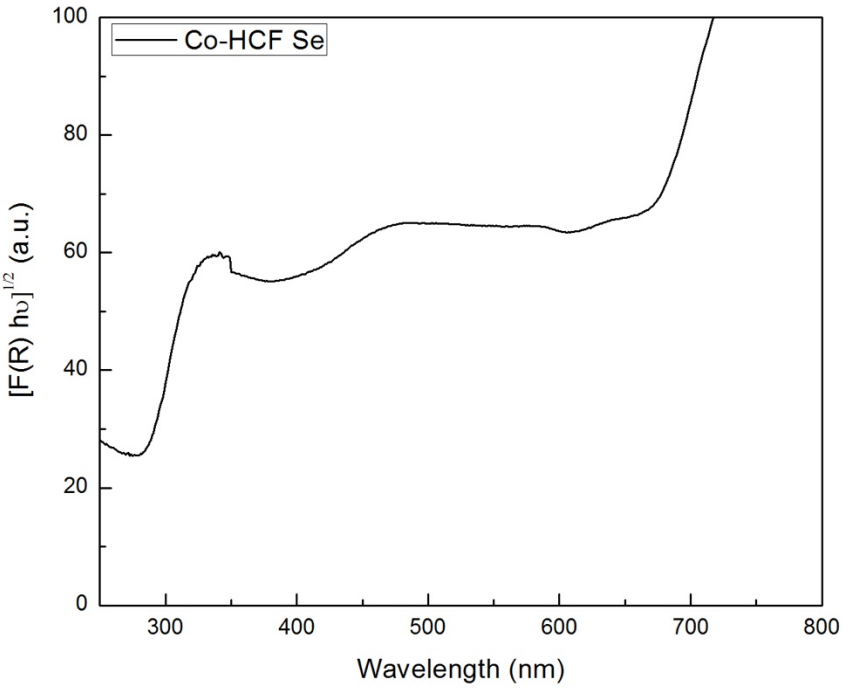

Figure 25. Optical reflectance spectrum of Co-HCF selenized sample.

From reflectance spectra in **Figure 24** and **25** respectively, it can be noticed that there is a small variation in the profile of the peaks of the two different samples. According to this optical result, they share a common absorption at about 350 nm, that was also observed in the Ni-HCF selenized sample.

The bandgap values for the samples under investigation were determined according to the method reported in Paragraph 3.1.1. In literature, it is reported an approximate value of 1.7 eV [85] for the bandgap of Co-HCF nanomaterials. The Tauc plots of the Co-HCF and Co-HCF selenized nanocubes are presented in **Figure 26** and **27**.

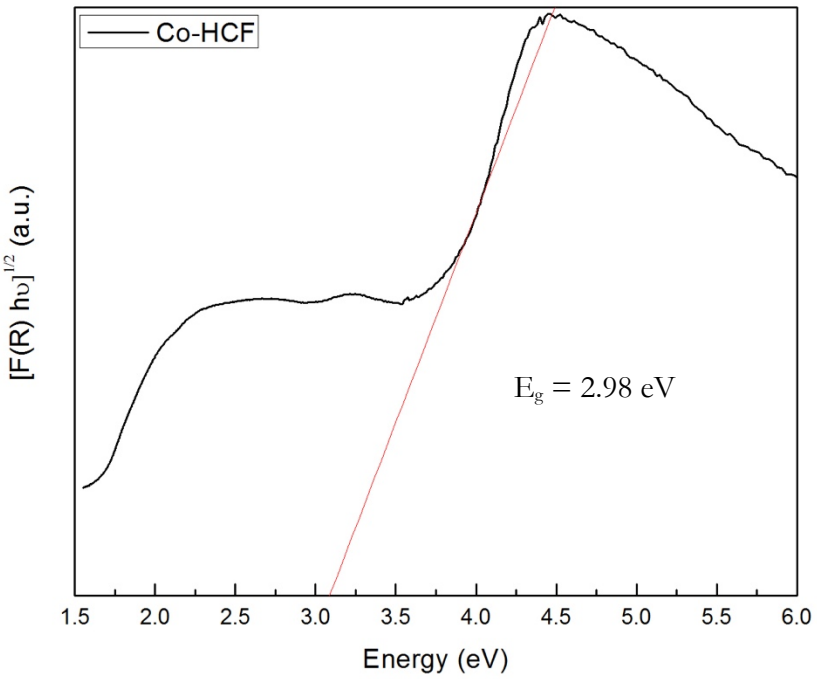

Figure 26. Tauc plot of Co-HCF sample.

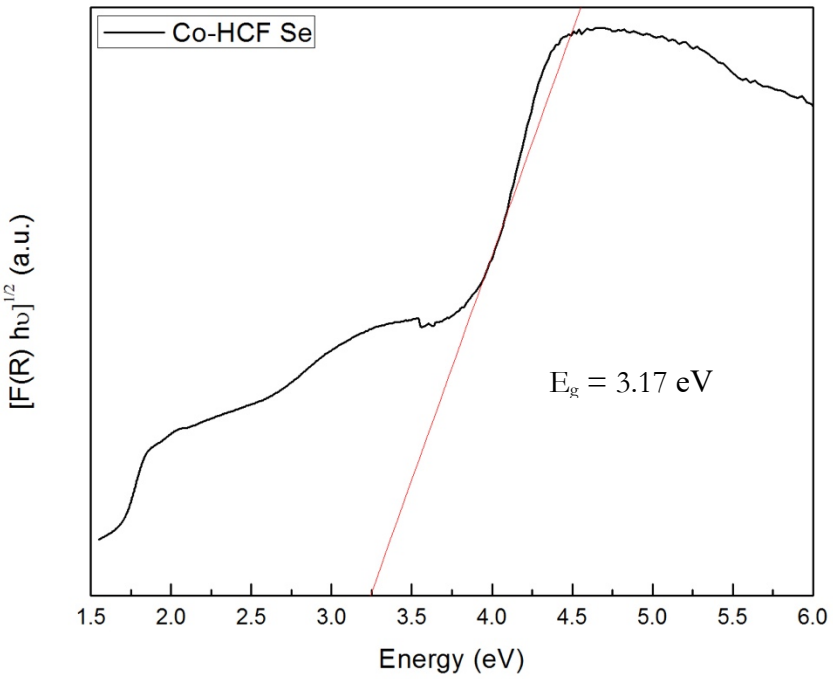

Figure 27. Tauc plot of Co-HCF selenized sample.

It can be observed that the profile of the selenized sample has been shifted towards higher energies in comparison to the pure Co-HCF sample. The meaning of these results is that selenization process tends

to broaden the band gap, as previously observed for the Ni-HCF-based nanomaterials. The Co-HCF sample shows a bandgap of 2.98 eV, while the selenized sample shows a bandgap of 3.17 eV. A comparison between experimental values obtained through this method and the values reported in the literature is reported in **Table 5**:

E_g Co-HCF (literature)	**E_g Co-HCF**	**E_g Co-HCF selenized**
1.7 eV [85]	2.98 eV	3.17 eV

Table 5. Comparison of the bandgap values obtained experimentally and from literature for Co-HCF-based samples.

4.2.2 X-ray Diffraction Analysis

The crystallographic structure of Co-HCF and Ni-HCF selenized samples has been revealed using an X-ray diffractometer with Cu Kα radiation in the range 2θ between 10° and 80°. The patterns of the samples are shown in **Figure 28**.

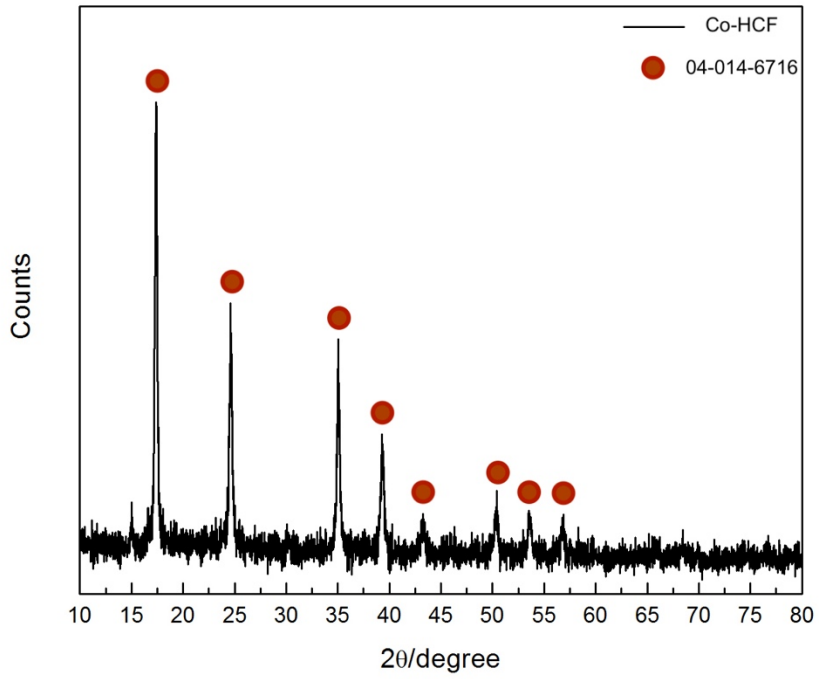

Figure 28. XRD pattern of Co-HCF sample.

The Co-HCF sample shows eight main peaks at a value 2θ of: 17.4°, 24.7°, 35.1°, 39.4°, 43.4°, 50.5°, 53.8°, and 57.0°. The peaks correspond to the cobalt iron cyanide phase (reference code: 04-014-6716, in dark-red). The peaks have been associated to the (200), (220), (400), (420), (422), (440), (600) and (620) peaks of the cobalt iron cyanide phase, respectively. According to the XRD pattern, it can be confirmed that the Co-HCF nanocubes show a pure crystalline structure, reconfirming the results reported in the literature. After that, the Co-HCF sample has been selenized. Its XRD profile is reported in **Figure 29**.

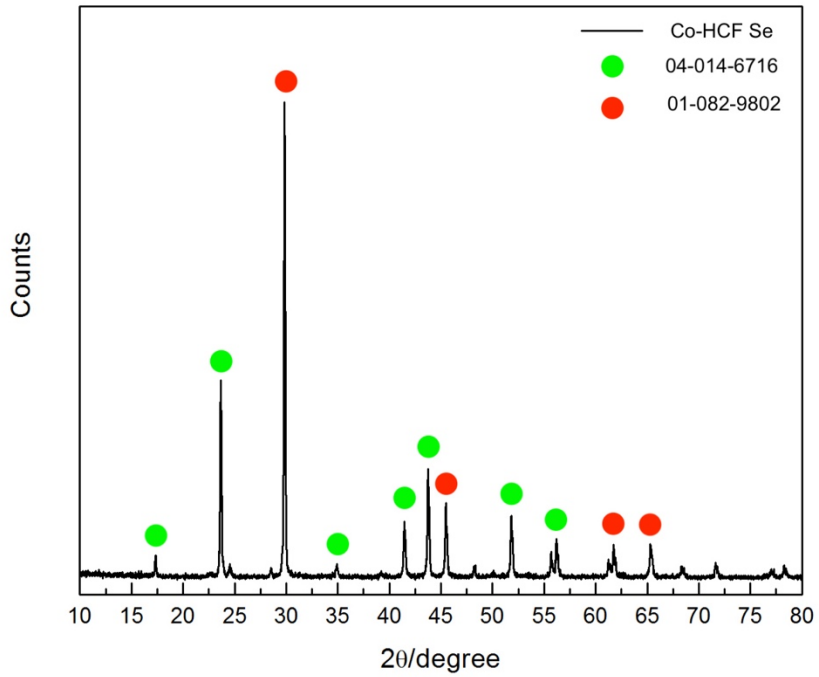

Figure 29. XRD pattern of Co-HCF selenized sample.

In addition to the characteristic peaks of cobalt iron cyanide, the selenization process adds 4 more peaks at 29.8°, 45.2°, 62.3° and 65.2° corresponding to (101), (022), (202) and (203) iron selenide peaks (reference code: 01-082-9802, in red), respectively.

These XRD results suggest that the Co-HCF inner core has been preserved during the selenization process and that in the meanwhile there was the formation of iron selenide. The selenization led on Co-HCF nanostructures brought to the generation of core-shell structures, where Co-HCF is the inner core and iron selenide is the outer shell. This can be further confirmed through EDS analysis.

4.2.3 Scanning Electron Microscopy

The morphological analysis of prepared nanocubes has been performed using a field-emission scanning electron microscope (FESEM). The micrographs of Co-HCF and Co-HCF selenized are shown in **Figure 30, 31** and **32**, respectively.

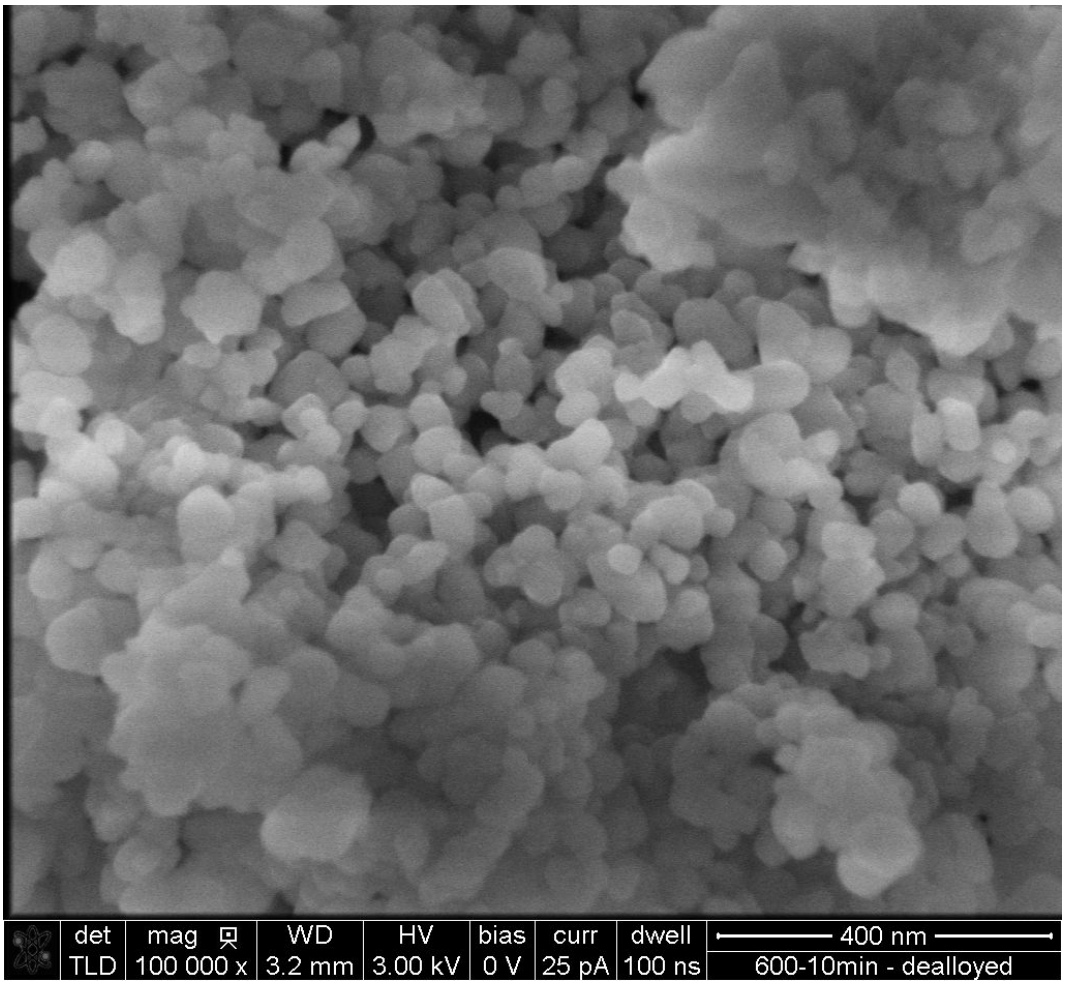

Figure 30. Morphology of Co-HCF sample.

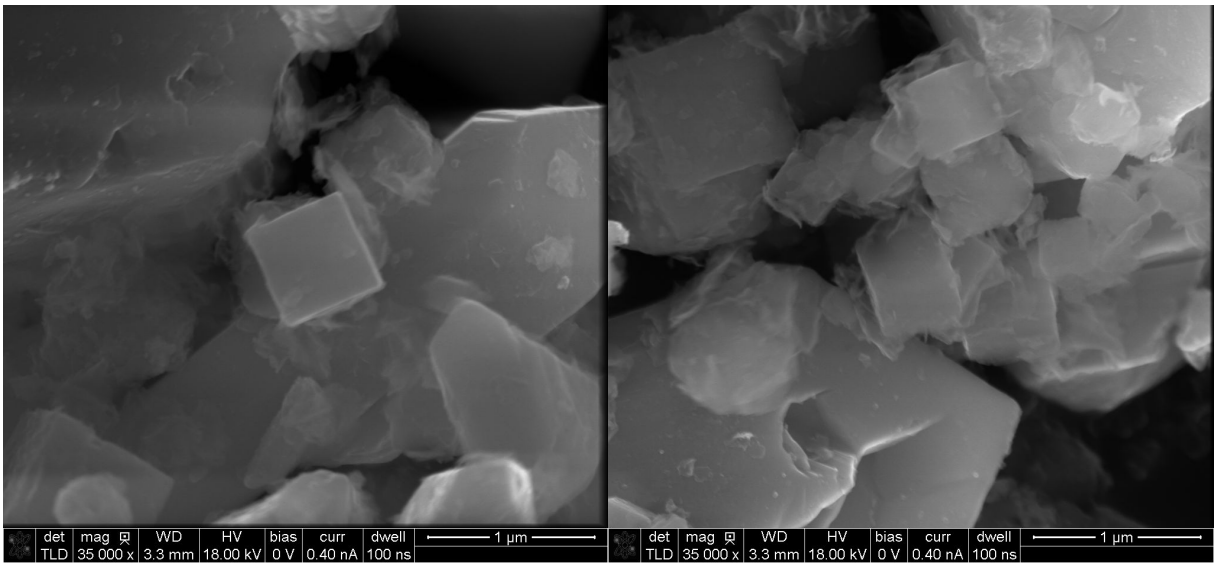

Figure 31 and 32. Morphology of Co-HCF selenized sample.

The same behavior shown previously for Ni-HCF-based nanomaterials has been observed in the Co-HCF-based samples, that is formation of random nanoparticles in the pure sample and formation of cubic nanostructures after the selenization process. The random nanoparticles obtained for the Co-HCF sample show an average dimension of 64 nm, while the same nanoparticles being selenized show a dimension of 619 nm (**Figure 31**), and a minimum and maximum of 285 nm and 491 nm, respectively (**Figure 32**).

This result reinforces the hypothesis from the previous case under investigation, confirming an overall positive influence of the selenization process on the system. In fact, nanoparticles turned from randomly shaped to cubic.

4.2.4. Energy Dispersive X-ray Spectroscopy

Energy dispersive X-ray spectrometric technique was used to determine the composition of the compounds. The following micrographs (**Figure 33, 34** and **35**) for the Co-HCF selenized nanocubes were obtained.

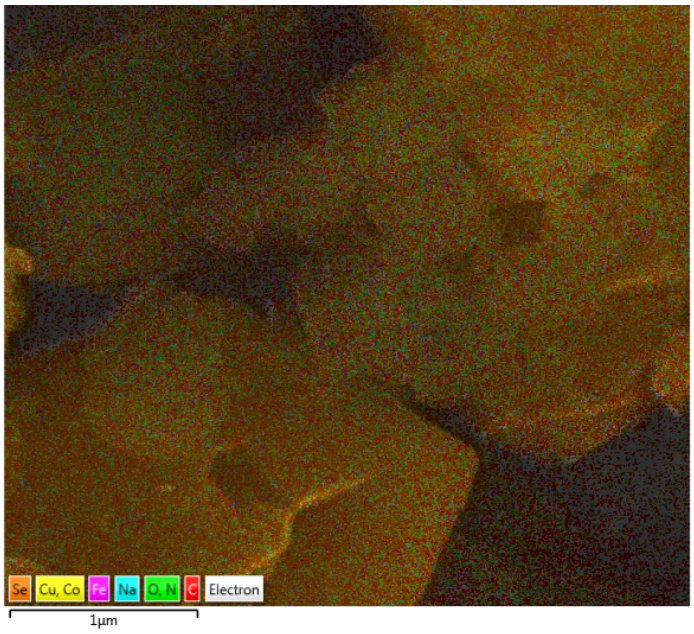

Figure 33. Elemental mapping of Co-HCF selenized sample.

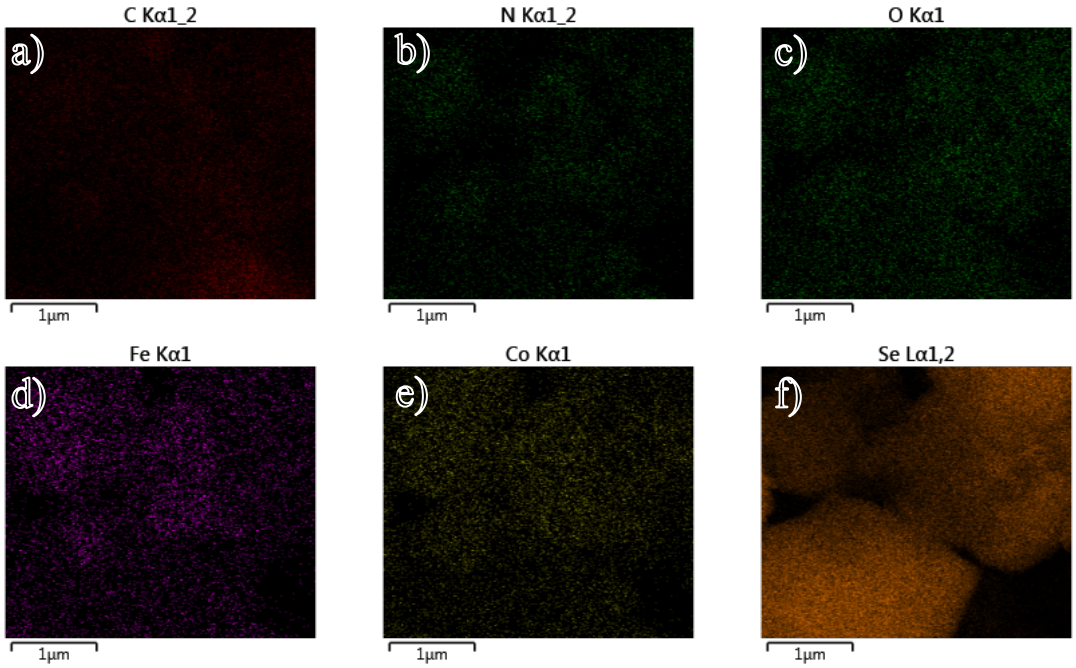

Figure 34. Elemental mapping of (a) carbon, (b) nitrogen, (c) oxygen, (d) iron, (e) cobalt and (f) selenium of Co-HCF selenized sample.

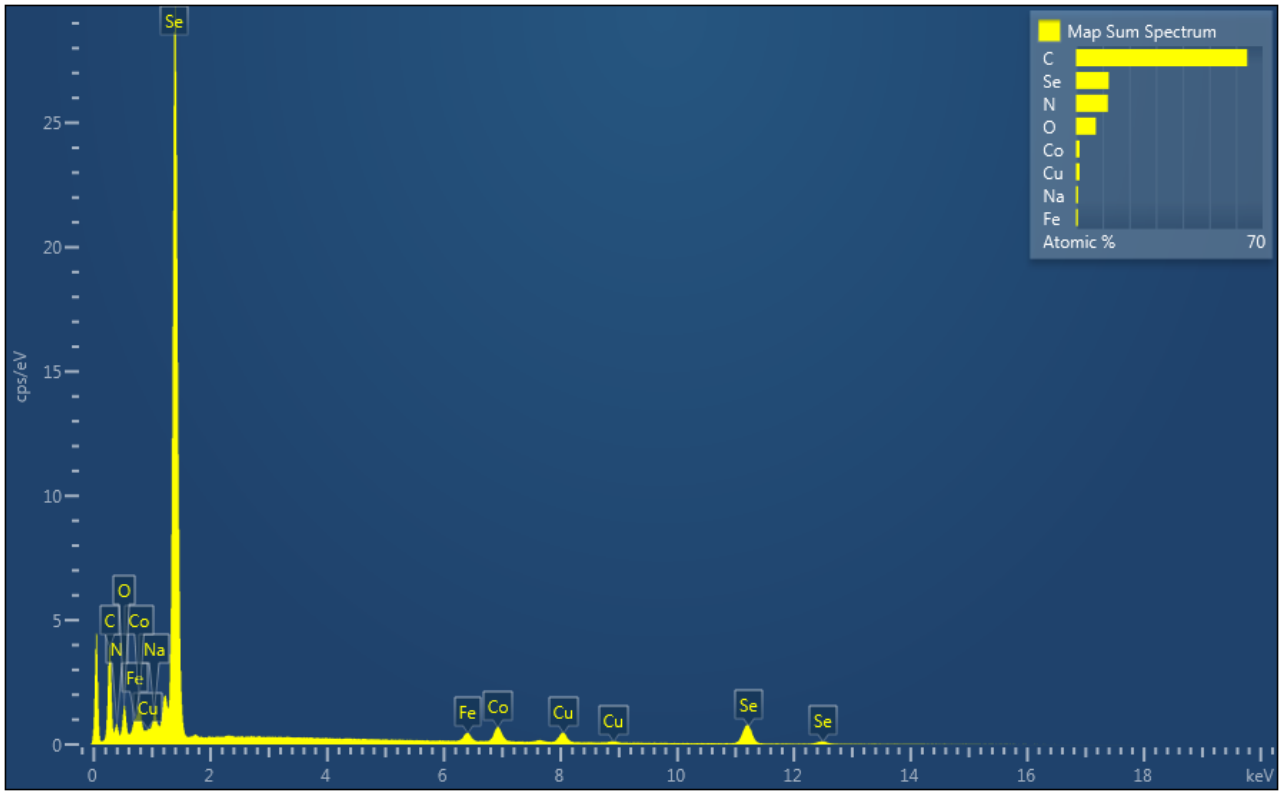

Figure 35. EDS graph of Co-HCF selenized sample.

From the EDS analysis the presence of carbon, oxygen, nitrogen, sodium, iron, cobalt, copper and selenium was detected, as confirmed by the EDS mapping in **Figure 33** as well. The signal coming from copper is related to the tape that to support the powder on the stabber. On the contrary, the signals coming from oxygen and sodium can be related to a not optimal washing of the samples after the centrifugation. Moreover, the presence of oxygen could be justified by the aforementioned malfunctioning of the pre-vacuum chamber of the microscope, by adsorbed oxygen molecules, or by partial surface oxidation (Paragraph 3.1.4).

Moreover, **Figure 35** makes it possible to observe the presence of both iron and selenium at the surface. EDS confirmed the formation of core-shell structures with Co-HCF cores and iron selenide shells, reinforcing the observations that were previously done. The selenization process affected the composition and the structure of the nanomaterials, and it generated core-shell nanocubes.

4.2.5. Fourier-Transform Infrared Spectroscopy

Infrared (IR) spectra were collected using a Vertex 80v The IR spectrum related to the Co-HCF sample is reported below (**Figure 36**).

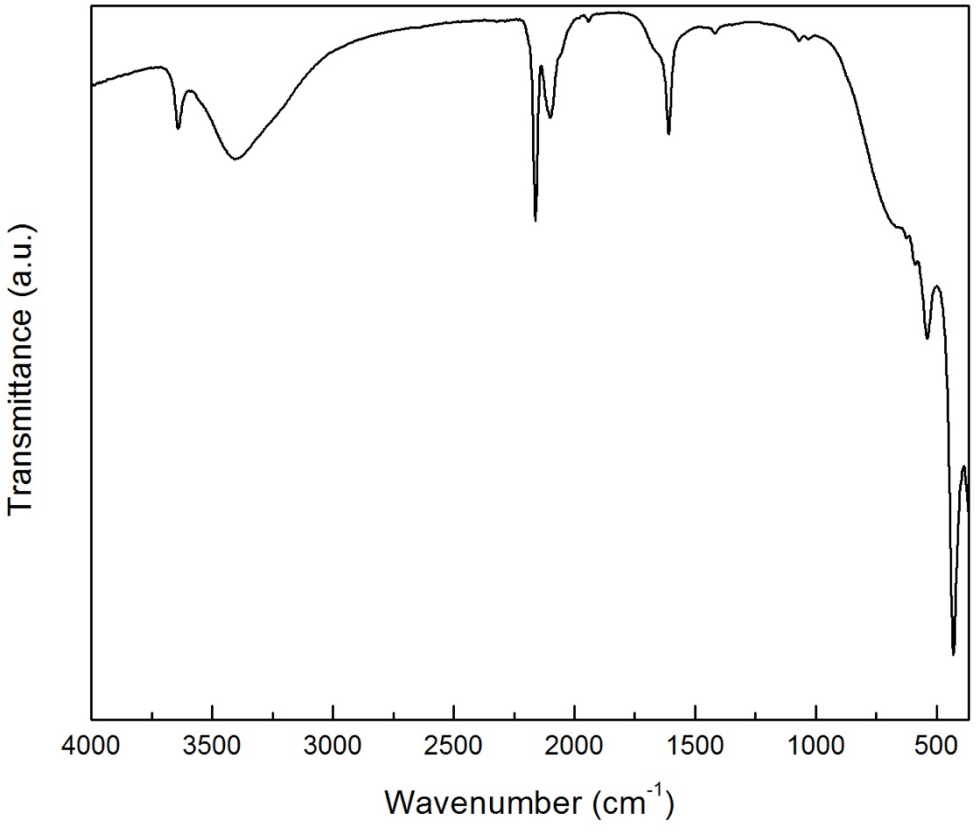

Figure 36. FTIR spectrum of Co-HCF sample.

Co-HCF spectrum is characterized by the presence of two major absorption peaks due to presence of CN groups and water molecules. The absorption band over the range of 2900-3740 cm^{-1} indicates the presence of -OH group. The presence of a sharp peak at 3643 cm^{-1} is attributable to strongly hydrogen bonded water molecule in the structure, as reported in literature [85]. The sharp peak at 2167 cm^{-1}, instead, corresponds to Fe^{III}-CN-Co^{II} linkages. Another less intense peak seen at 2093 cm^{-1} arises probably due to unreacted potassium ferricyanide or Fe^{II}-CN-Co^{II} linkage. To further understand which of the two possibilities is responsible for this signal, XPS analysis could help in order to understand if there is the presence of Fe(II) valence state in the compound. In the range between 425 cm^{-1} and 544 cm^{-1} the presence of Co-C stretching and Co-CN bending is observed.

Unfortunately, no IR spectra of the Co-HCF selenized sample could have been acquired to determine the effect of the selenization on the structure.

4.2.6. Electrochemical measurements

The performances of Co-HCF and Co-HCF selenized nanocubes were studied as electrode materials for oxygen evolution reaction using a three-electrode set up.

To evaluate their OER activity, the Co-based materials were loaded onto glassy carbon (GC) and investigated using electrochemical linear sweep voltammetry (LSV), electrochemical impedance spectroscopy (EIS) and cyclic voltammetry (CV) technique in 1 M KOH (pH 14) electrolyte.
The electrocatalytic activity of Co-HCF and Co-HCF selenized for OER was firstly evaluated through linear sweep voltammetry. **Figure 37** shows the LSV curves for the two electrocatalysts under investigation.

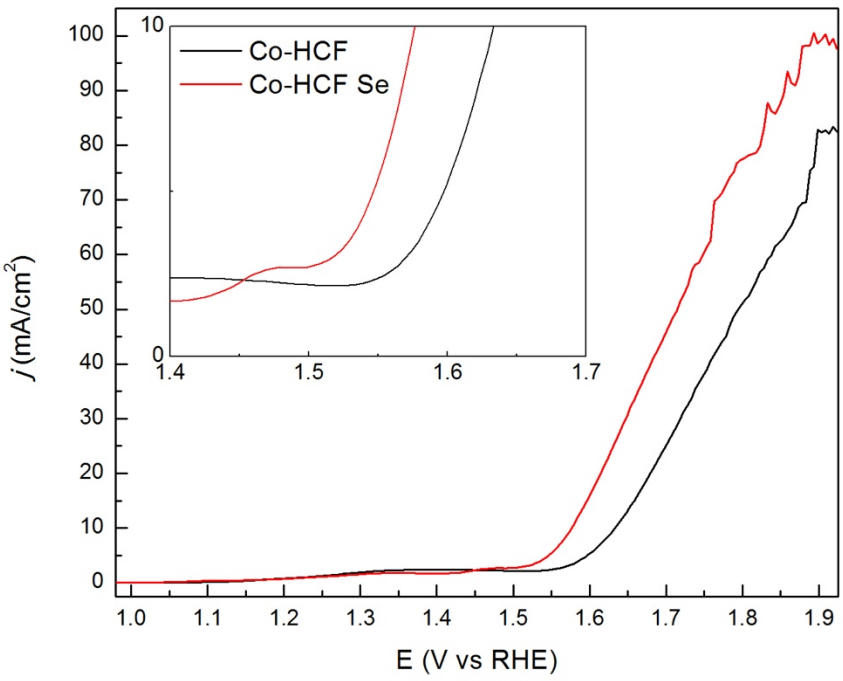

Figure 37. Linear sweep voltammetry curves of Ni-HCF and Ni-HCF selenized samples with magnification from 1.4 V to 1.7 V (vs RHE).

The Co-HCF selenized nanocubes exhibit enhanced electrocatalytic performance compared to the bare counterpart. The selenized sample shows the lowest overpotential of 340 mV (vs RHE) at a current density of 10 mA/cm^2, which is much lower than the non-selenized sample (400 mV vs RHE). In addition, the selenized electrocatalyst exhibits the smallest onset overpotential (at 2.5 V vs RHE), that is 280 mV (vs RHE) compared to bare Co-HCF that shows an onset potential of 340 mV (vs RHE).

Another result that must be highlighted is the current density of the samples measured at 1.9 V (vs RHE). The selenized sample can reach reaches 99 mA/cm^2 at 1.9 V (vs RHE), which is 1.2 times higher than that of bare Co-HCF counterpart that reaches 83 mA/cm^2 at 1.9 V (vs RHE).

Also for these samples, the Tafel slopes have been calculated to evaluate the OER catalytic kinetics. The Tafel plots of Co-HCF and Co-HCF selenized nanocubes were derived from LSV curves by fitting the linear regions according to the Tafel equation. The corresponding results are shown in **Figure 38** and **39**.

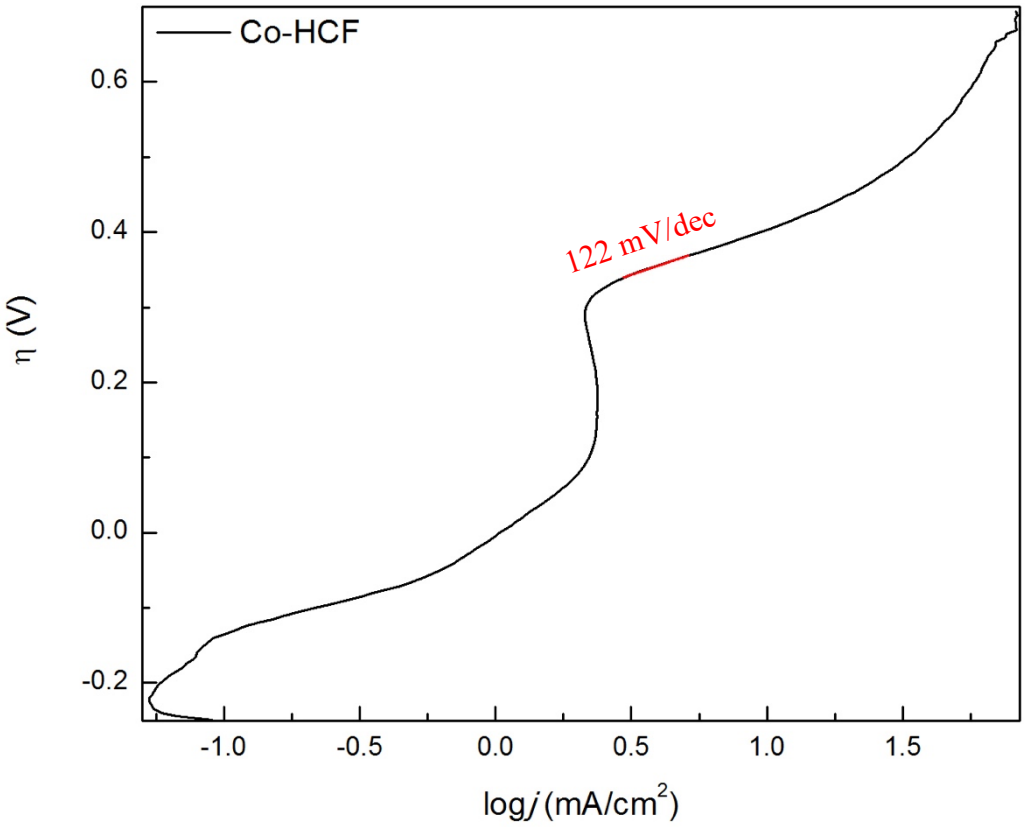

Figure 38. Tafel plot of Co-HCF sample.

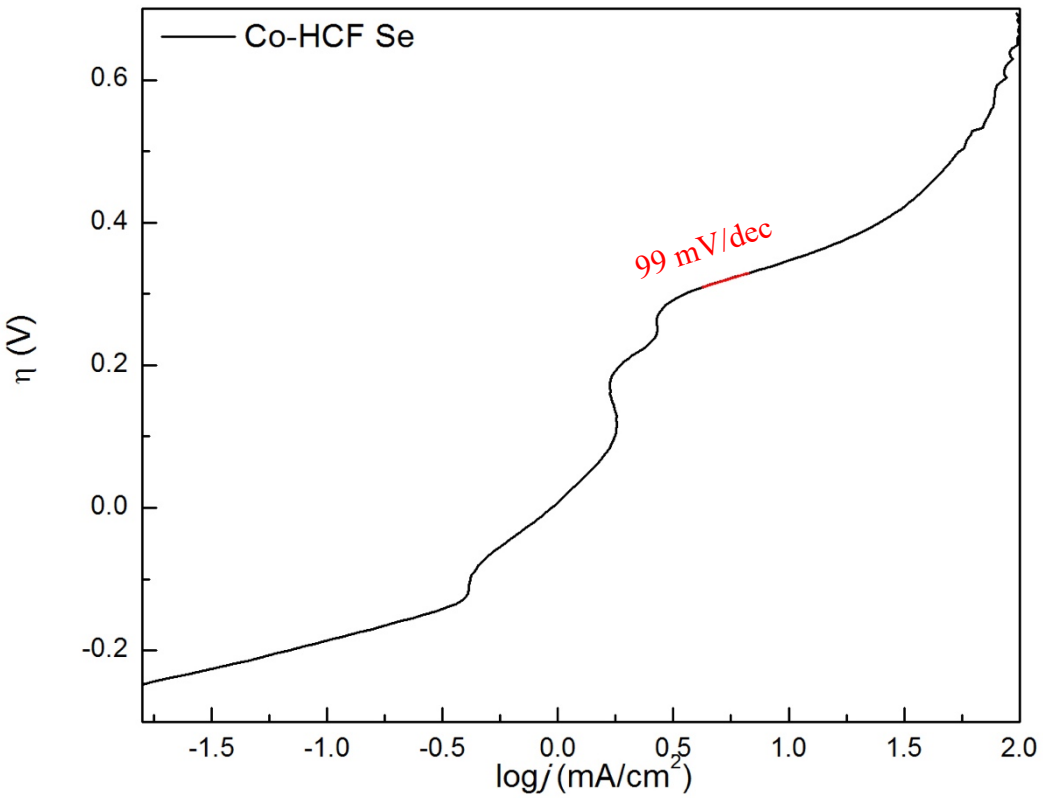

Figure 39. Tafel plot of Co-HCF selenized sample.

From the Tafel plots, it can be observed that the selenized Co-HCF nanocubes show a Tafel slope of 99 mV dec^{-1}, a smaller value compared to the one obtained for bare Co-HCF (122 mV dec^{-1}). It is preferred having a low Tafel slope value in order to have lower overpotentials and high current density values in OER and this is actually what happens for the selenized sample. As in the case of Ni-HCF selenized sample previously reported, the selenization improved the catalytic activity of the nanomaterials in OER and enhanced the charge transfer rate. The reason for this behavior can be attributed to the formation of a core-shell structure that has been previously proved by EDS and XRD analysis.

The list of the results (**Table 6**) shows that the selenization process yielded into higher performances compared to the bare Co-HCF.

Material	Onset potential @2.5 mA/cm² (mV)	Reported onset potential (mV)	Tafel slope (mV/dec)	Reported Tafel slope (mV/dec)
Co-HCF	340	350	122	146 [85]
Co-HCF selenized	280	-	99	-

Table 6. Summary of the main parameters according to LSV analysis for Co-HCF and Co-HCF selenized samples.

In order to further investigate how the selenization process affects the OER electrocatalytic performance compared to bare Ni-HCF nanoparticles, the electrochemically active surface areas of the samples were assessed by the electrochemical double-layer capacitance (C_{dl}) acquired through CV tests at the different scan rates (**Figure 40, 41** and **42**).

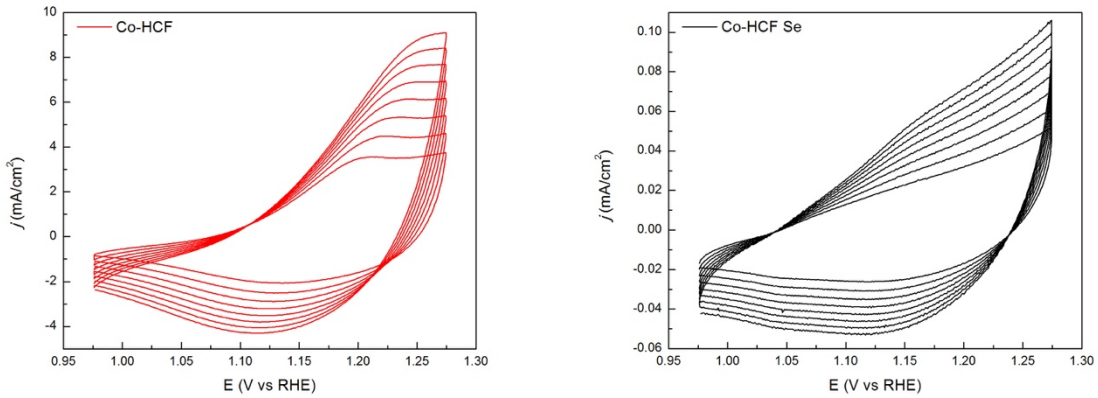

Figure 40 (left) and 41 (right). CV curves of Co-HCF (left) and Co-HCF selenized (right) catalysts at different scan rates.

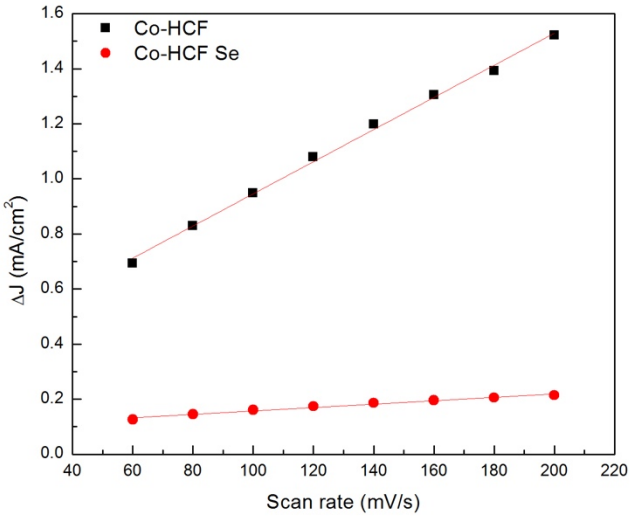

Figure 42. Linear plots of double-layer current as a function of the scan rate for Co-HCF (black) and Co-HCF selenized (red).

What can be observed from the CV curves reported is that the current density of selenized Co-HCF electrocatalyst is much lower in comparison to that of bare Co-HCF electrocatalyst. Instead, as seen in **Figure 42**, the C_{dl} value of bare Co-HCF selenized (5.8 mF cm^{-2}) is about 9.4 times higher than selenized Co-HCF nanoparticles (0.62 mF cm^{-2}), demonstrating that the selenized sample possesses lower ECSA, even if Tafel slope parameter highlights a faster kinetics in the case of the selenized sample.

In addition to LSV and CV, electrochemical impedance spectroscopy (EIS) of Co-HCF and Co-HCF selenized was tested at a constant potential of 550 mV (vs. RHE) to further understand the features of these samples. The Nyquist plots of bare Co-HCF (**Figure 43**) and Co-HCF selenized (**Figure 44**) are presented below.

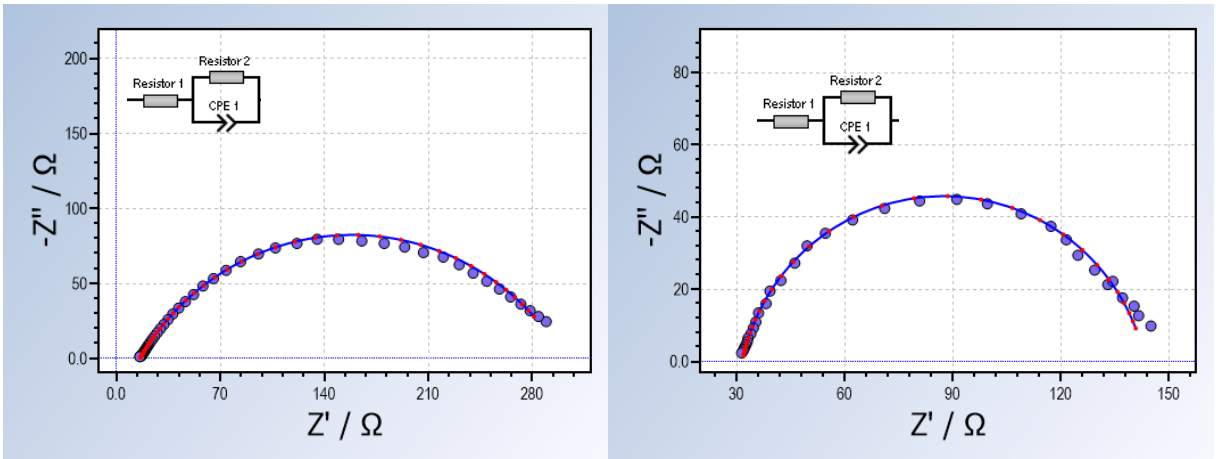

Figure 43 and 44. Nyquist plots of Co-HCF (left) and Co-HCF selenized (right) in 1.0 M KOH electrolyte at the potential of 550 mV.

As in the previous case for Ni-HCF-based nanomaterials, also in here the Nyquist plots of the samples consist of a semicircle. The insets represent the equivalent circuits used to obtain the charge transfer resistance of the OER catalysts. The parameters to calculate the capacitance were obtained using RelaxIS 3 software fitting the equivalent circuit in order to give an interpretation of the reaction kinetics [63,64].

The corresponding values are listed in **Table 7**:

Material	Resistance 1 (Ω)	Resistance 2 (Ω)	CPE (S-sec$^{0.5}$)	α (0 < α < 1)
Co-HCF	31.52	111.9	0.00480	0.873
Co-HCF selenized	15.62	286.0	0.00098	0.666

Table 7. Simulated values of resistance (R_1 and R_2), capacitance (CPE) and α of EIS spectra calculated by equivalent circuit through RelaxIS 3 software.

Where "Resistance 1" and "Resistance 2" are related to the equivalent circuit used for the fitting, CPE is the capacitance and α. The capacitance values have been calculated as done for the previous case, using the following formula:

$$C = (Q(R_1)^{(1-\alpha)})^{\frac{1}{\alpha}}$$

According to these results, the non-selenized sample shows a strong capacitor behavior, confirming the supercapacitors behavior of Co-HCF reported in the literature. On the other hand, the selenized sample is more likely to show a capacitor behavior rather than a resistor one.

5. Conclusions

This thesis provides a simple and facile approach to synthesize selenium-based nanostructures through a protocol that has not been reported in literature yet. The protocol consists of two steps: (i) one-pot synthetic reaction with a subsequent (ii) selenization process. In the first step, nickel HCFs (Ni-HCFs) and cobalt HCFs (Co-HCFs) nanoparticles have been obtained by a facile synthesis involving potassium ferricyanide ($K_3Fe(CN)_6$) and, according to the desired metal, Ni and Co salts.
In the second step, the selenization process has been led using NaHSe, allowing to obtain selenium-based selenium-based core-shell nanostructures for water splitting application. The confirmation came from Scanning Electron Microscopy, Fourier-Transform Infrared spectroscopy and reaffirmed by X-ray Diffraction analysis. In the latter case, only the Co-HCF have been demonstrated to have a pure crystalline structure, while the other samples under investigation have shown a composite phase. The fact that some samples developed a core-shell structure could have enhanced the performances in oxygen evolution reaction, because in this kind of mechanism the catalytic sites undergo continuous cycles of oxidation and reduction as soon as they pass from the adsorption of water molecules to the evolution of oxygen. This requires a degree of flexibility in the ability to reorganize the structure that is usually not present in pure crystalline structures, making the composite phases more refined.

The influence that the selenization process has on the samples has been deeply investigated. From UV-Vis measurements it appears that the presence of selenide in the outer structures broadens the band gap. This is more evident in the case of Ni-HCF and Ni-HCF selenized samples: the selenization process broadens the band gap turning from 1.97 eV to 2.67 eV. On the other hand, the Co-HCF-based samples showed a discrepancy of 0.19 eV, allowing to conclude that the selenization process exerts influence in a softer way with respect to Ni-based nanomaterials.

Electrochemical measurements with a three-electrode configuration were led through potentiostatic analysis which made it possible to study the performances of these materials for OER. The Ni-HCF-based nanomaterials have been demonstrated to have remarkable efficiencies in OER. Further, these samples exhibit the lowest Tafel slope value (33 mV/dec) showing the faster kinetics towards OER. This value is 5 times smaller with respect to the unselenized sample and 1.3 times smaller than the best result reported in literature, a result obtained using more complex structures and more complex synthesis protocols. The same can be said of Co-HCF selenized core-shell nanocubes, where their Tafel slope reached values of 99 mV/dec, that are much lower than bare samples (122 mV/dec) and similar compounds reported in literature (150 mV/dec). This allows to conclude that the selenization process can effectively adjust the composition and the structure of the as-fabricated catalysts, accelerating the kinetics of the reaction and, hence, improving the electrocatalytic activity in oxygen evolution reaction.

Based on the above reported results and discussions, the enhanced performances in OER can be ascribed to the following two aspects: (i) the insertion of selenium in the nanostructures made the compounds even more electron rich and this guaranteed a higher conductivity, surface activity and more active catalytic sites; (ii) the presence of selenium seems to promote the charge transfer at the interface between electrode and electrocatalyst due to a relatively low transfer resistance.

This project offers a new idea for designing and exploiting earth-abundant elements based nanomaterials for the development of cheap and efficient electrocatalysts for water splitting.

Further investigations could be useful to investigate in-depth the properties and which parameters can be changed to obtain even more efficient catalysts. An example could be X-ray Photoelectron Spectroscopy (XPS), through which it is possible to determine the presence of Fe(II) valence states in the compound that could somehow affect the performances. Using the same technique, it could be interesting to determine the electronic structures that arise from the coupling of cubic PBAs and selenium elements and how the electronic structure influences the activities of the catalytic sites. Rotating Ring Disk Electrode (RRDE) could be used as well to determine the Faradaic efficiency, in order to understand the selectivity of the catalysts, since in HER and OER by-products could compete in the reaction.

Summarizing, a new protocol for the preparation of core-shell selenium-based nanocubes has been achieved with remarkable results. These products, due to a facile synthesis method and to very fast kinetics in OER, could be scaled-up in the production, substituting conventional noble-metal catalysts with cheaper and more abundant composite nanostructures.

6. Acknowledgements

This work would not have been possible without the patience, the support and the friendship of all those people that I had the good fortune to know and to collaborate with. With these few lines I want to express my warmest thanks to all of them.

To Professor Elisa Moretti and Professor Vomiero: I could not have asked for better supervisors. You guided me through all my project, supporting me and suggesting me always in the best way possible. But more than the scientific point of view, I would like to thank you for inspiring me as people. If someone will ever ask me what I will be when I grow, my answer would be "You".

To Professor Isabella Concina, for the discussions and for helping me planning my project in Sweden. Thank you for making me appreciate this wonderful country.

To Kamran, for his support and the scientific contributions to this thesis, but also for the many inspiring debates on music, politics and everything else.

To Getachew, Moji, Tofik, Kashinath and all the people from LTU. Without you every characterization would not have been possible. But I would like to say that the most import thing I learnt from you is that there is no science without having fun.

To Letizia and Nicolò, for the coffee breaks, for the Friday Beer, for the endless jokes, for everything. You have always been so available and you have always been there for me, I am glad that during my internship I had the opportunity to start this new Friendship.

To Matteo, Sandro and Saimir: you have been the best fellows. You made me rediscover the true meaning of "friends" and I will never be able to thank you enough for all the things you have done for me. Long live the "becana"!

Out of the workplace, I want to thank my Great Love: Carolina. You believed in me when I was not able to believe in it either. You made me a better person, loving me every single day. All of this is priceless.

And finally you: Mom and Dad. You always pushed me to follow my dreams and I will do everything I can to make your dreams come true. I learnt the most precious lessons from you, I will never be grateful enough!

"It is the small things,
everyday deeds of ordinary folk that keeps the darkness at bay.
Simple acts of kindness and love"

J. R. R. Tolkien

7. References

[1] M. A. Méndez, R. Partovi-Nia, I. Hatay, B. Su, P. Ge, A. Olaya, N. Younan, M. Hojeij, H. H. Girault, "Molecular electrocatalysis at soft interfaces," *Phys. Chem. Chem. Phys.*, vol. 12, no. 46, pp. 15163–15171, 2010, doi: 10.1039/c0cp00590h.

[2] E. Kusmierek, "Semiconductor electrode materials applied in photoelectrocatalytic wastewater treatment—An overview," *Catalysts*, vol. 10, no. 4, pp. 1–49, 2020, doi: 10.3390/catal10040439.

[3] C. F. Zinola, M. E. Martins, E. P. Tejera, N. P. Neves, "Electrocatalysis: Fundamentals and Applications," *Int. J. Electrochem.*, vol. 2012, pp. 1–2, 2012, doi: 10.1155/2012/874687.

[4] A. J. Appleby, "Electrocatalysis and Fuel Cells," *Catalysis Reviews: Science and Engineering*, no. November 2012, pp. 37–41, 2006.

[5] N. Fujiwara, K. A. Friedrich, U. Stimming, "Ethanol oxidation on PtRu electrodes studied by differential electrochemical mass spectrometry," *J. Electroanal. Chem.*, vol. 472, no. 2, pp. 120–125, 1999, doi: 10.1016/S0022-0728(99)00282-X.

[6] S. Pérez-Rodríguez, F. Barreras, E. Pastor, M. J. Lázaro, "Electrochemical reactors for CO2 reduction: From acid media to gas phase," *Int. J. Hydrogen Energy*, vol. 41, no. 43, pp. 19756–19765, 2016, doi: 10.1016/j.ijhydene.2016.06.130.

[7] C. X. Zhao, B. Q. Li, M. Zhao, J. N. Liu, L. D. Zhao, X. Chen, Q. Zhang, "Precise anionic regulation of NiFe hydroxysulfide assisted by electrochemical reactions for efficient electrocatalysis," *Energy Environ. Sci.*, vol. 13, no. 6, pp. 1711–1716, 2020, doi: 10.1039/c9ee03573g.

[8] M. Sakthivel, R. Sukanya, S. M. Chen, K. Pandi, K. C. Ho, "Synthesis and characterization of bimetallic nickel-cobalt chalcogenides (NiCoSe2, NiCo2S4, and NiCo2O4) for non-enzymatic hydrogen peroxide sensor and energy storage: Electrochemical properties dependence on the metal-to-chalcogen composition," *Renew. Energy*, vol. 138, pp. 139–151, 2019, doi: 10.1016/j.renene.2019.01.079.

[9] P. Zelenay, J. H. Choi, C. M. Johnston, D. Cao, P. K. Babu, A. Wieckowski, N. Alonso-Vante, "Oxygen Reduction Electrocatalysis at Chalcogen-Modified Ruthenium Cathodes," *ECS Trans.*, vol. 3, no. 1, pp. 171–179, 2019, doi: 10.1149/1.2356135.

[10] Q. Wang, Y. Lei, Y. Zhu, H. Wang, J. Feng, G. Ma, Y. Wang, Y. Li, B. Nan, Q. Feng, Z. Lu, H. Yu, "Edge Defect Engineering of Nitrogen-Doped Carbon for Oxygen Electrocatalysts in Zn-Air Batteries," *ACS Appl. Mater. Interfaces*, vol. 10, no. 35, pp. 29448–29456, 2018, doi: 10.1021/acsami.8b07863.

[11] J. C. Cruz, V. Baglio, S. Siracusano, R. Ornelas, L. Ortiz-Frade, L. G. Arriaga, V. Antonucci, A. S. Aricò, "Nanosized IrO2 electrocatalysts for oxygen evolution reaction in an SPE electrolyzer," *J. Nanoparticle Res.*, vol. 13, no. 4, pp. 1639–1646, 2011, doi: 10.1007/s11051-010-9917-2.

[12] T. Wu, B. H. Nguyen, M. C. Daugherty, K. D. Moeller, "Paired Electrochemical Reactions and the On-Site Generation of a Chemical Reagent," *Angew. Chemie*, vol. 131, no. 11, pp. 3600–3603, 2019, doi: 10.1002/ange.201900343.

[13] B. A. Frontana-Uribe, R. D. Little, J. G. Ibanez, A. Palma, R. Vasquez-Medrano, "Organic electrosynthesis: A promising green methodology in organic chemistry," *Green Chem.*, vol. 12, no. 12, pp. 2099–2119, 2010, doi: 10.1039/c0gc00382d.

[14] M. Gaberscek, J. Moskon, B. Erjavec, R. Dominko, J. Jamnik, "The importance of interphase contacts in Li ion electrodes: The meaning of the high-frequency impedance arc," *Electrochem. Solid-State Lett.*, vol. 11, no. 10, pp. 170–174, 2008, doi: 10.1149/1.2964220.

[15] E. Roduner, S. G. Radhakrishnan, "In command of non-equilibrium," *Chem. Soc. Rev.*, vol. 45, no. 10, pp. 2768–2784, 2016, doi: 10.1039/c6cs00115g.

[16] K. Sasaki, H. Naohara, Y. Cai, Y. M. Choi, P. Liu, M. B. Vukmirovic, J. X. Wang, R. R. Adzic, "Core-Protected Platinum Monolayer Shell High-Stability Electrocatalysts for Fuel-Cell Cathodes," *Angew. Chemie*, vol. 122, no. 46, pp. 8784–8789, 2010, doi: 10.1002/ange.201004287.

[17] K. B. Li, D. W. Shi, Z. Y. Cai, G. L. Zhang, Q. A. Juang, D. Liu, C. P. Yang, "Studies on the equivalent serial resistance of carbon supercapacitor," *Electrochim. Acta*, vol. 174, pp. 596–600, 2015, doi: 10.1016/j.electacta.2015.06.008.

[18] P. Gao, M. J. Weaver, "Metal-adsorbate vibrational frequencies as a probe of surface bonding: Halides and pseudohalides at gold electrodes," *J. Phys. Chem.*, vol. 90, no. 17, pp. 4057–4063, 1986, doi: 10.1021/j100408a045.

[19] P. O. Bedolla, G. Feldbauer, M. Wolloch, S. J. Eder, N. Dörr, P. Mohn, J. Redinger, A. Vernes, "Effects of van der Waals interactions in the adsorption of isooctane and ethanol on Fe(100) surfaces," *J. Phys. Chem. C*, vol. 118, no. 31, pp. 17608–17615, 2014, doi: 10.1021/jp503829c.

[20] K. P. Kuhl, E. R. Cave, D. N. Abram, T. F. Jaramillo, "New insights into the electrochemical reduction of carbon dioxide on metallic copper surfaces," *Energy Environ. Sci.*, vol. 5, no. 5, pp. 7050–7059, 2012, doi: 10.1039/c2ee21234j.

[21] E. V. Kondratenko, G. Mul, J. Baltrusaitis, G. O. Larrazábal, J. Pérez-Ramírez, "Status and perspectives of CO2 conversion into fuels and chemicals by catalytic, photocatalytic and electrocatalytic processes," *Energy Environ. Sci.*, vol. 6, no. 11, pp. 3112–3135, 2013, doi:

10.1039/c3ee41272e.

[22] J. Wu, S. Ma, J. Sun, J. I. Gold, C. Tiwary, B. Kim, L. Zhu, N. Chopra, I. N. Odeh, R. Vajtai, A. Z. Yu, R. Luo, J. Lou, G. Ding, P. J. A. Kenis, P. M. Ajayan, "A metal-free electrocatalyst for carbon dioxide reduction to multi-carbon hydrocarbons and oxygenates," *Nat. Commun.*, vol. 7, pp. 1–6, 2016, doi: 10.1038/ncomms13869.

[23] I. C. Sena, D. O. Sales, T. S. Andrade, M. Rodriguez, A. C. da Silva, F. G. E. Nogueira, J. L. Rodrigues, J. P. de Mesquita, M. C. Pereira, "Photoassisted chemical energy conversion into electricity using a sulfite-iron photocatalytic fuel cell," *J. Electroanal. Chem.*, vol. 881, pp. 2–11, 2021, doi: 10.1016/j.jelechem.2020.114940.

[24] S. Cherevko, A. R. Zeradjanin, A. A. Topalov, N. Kulyk, I. Katsounaros, K. J. J. Mayrhofer, "Dissolution of noble metals during oxygen evolution in acidic media," *ChemCatChem*, vol. 6, no. 8, pp. 2219–2223, 2014, doi: 10.1002/cctc.201402194.

[25] S. Anantharaj, S. Kundu, "Do the Evaluation Parameters Reflect Intrinsic Activity of Electrocatalysts in Electrochemical Water Splitting?," *ACS Energy Lett.*, vol. 4, no. 6, pp. 1260–1264, 2019, doi: 10.1021/acsenergylett.9b00686.

[26] S. Anantharaj, S. R. Ede, K. Sakthikumar, K. Karthick, S. Mishra, S. Kundu, "Recent Trends and Perspectives in Electrochemical Water Splitting with an Emphasis on Sulfide, Selenide, and Phosphide Catalysts of Fe, Co, and Ni: A Review," *ACS Catal.*, vol. 6, no. 12, pp. 8069–8097, 2016, doi: 10.1021/acscatal.6b02479.

[27] E. Gileadi, E. Kirowa-Eisner, "Some observations concerning the Tafel equation and its relevance to charge transfer in corrosion," *Corros. Sci.*, vol. 47, no. 12, pp. 3068–3085, 2005, doi: 10.1016/j.corsci.2005.05.044.

[28] E. Fabbri, A. Habereder, K. Waltar, R. Kötz, T. J. Schmidt, "Developments and perspectives of oxide-based catalysts for the oxygen evolution reaction," *Catal. Sci. Technol.*, vol. 4, no. 11, pp. 3800–3821, 2014, doi: 10.1039/c4cy00669k.

[29] J. Kibsgaard, T. F. Jaramillo, F. Besenbacher, "Building an appropriate active-site motif into a hydrogen-evolution catalyst with thiomolybdate [Mo3S13]2- clusters," *Nat. Chem.*, vol. 6, no. 3, pp. 248–253, 2014, doi: 10.1038/nchem.1853.

[30] S. Anantharaj, M. Jayachandran, S. Kundu, "Unprotected and interconnected Ru0 nano-chain networks: Advantages of unprotected surfaces in catalysis and electrocatalysis," *Chem. Sci.*, vol. 7, no. 5, pp. 3188–3205, 2016, doi: 10.1039/c5sc04714e.

[31] P. Moreno-Garciá, N. Kovács, V. Grozovski, M. D. J. Gálvez-Vázquez, S. Vesztergom, P. Broekmann, "Toward CO2 Electroreduction under Controlled Mass Flow Conditions: A

Combined Inverted RDE and Gas Chromatography Approach," *Anal. Chem.*, vol. 92, no. 6, pp. 4301–4308, 2020, doi: 10.1021/acs.analchem.9b04999.

[32] I. S. Filimonenkov, S. Y. Istomin, E. V. Antipov, G. A. Tsirlina, E. R. Savinova, "Rotating ring-disk electrode as a quantitative tool for the investigation of the oxygen evolution reaction," *Electrochim. Acta*, vol. 286, pp. 304–312, 2018, doi: 10.1016/j.electacta.2018.08.056.

[33] J. J. H. Pijpers, M. T. Winkler, Y. Surendranath, T. Buonassisi, D. G. Nocera, "Light-induced water oxidation at silicon electrodes functionalized with a cobalt oxygen-evolving catalyst," *Proc. Natl. Acad. Sci. U. S. A.*, vol. 108, no. 25, pp. 10056–10061, 2011, doi: 10.1073/pnas.1106545108.

[34] S. Khajavi, J. C. Jansen, F. Kapteijn, "Production of ultra pure water by desalination of seawater using a hydroxy sodalite membrane," *J. Memb. Sci.*, vol. 356, no. 1–2, pp. 52–57, 2010, doi: 10.1016/j.memsci.2010.03.026.

[35] F. Ambrosio, J. Wiktor, A. Pasquarello, "PH-Dependent Catalytic Reaction Pathway for Water Splitting at the BiVO4-Water Interface from the Band Alignment," *ACS Energy Lett.*, vol. 3, no. 4, pp. 829–834, 2018, doi: 10.1021/acsenergylett.8b00104.

[36] B. J. Wiersma, "Hydrogen Generation During the Corrosion of Carbon Steel in Oxalic Acid," vol. 00441, no. December, pp. 1–21, 2004.

[37] A. Kabza, "Fuel Cell Formulary Contents," 2013.

[38] Y. Tachibana, L. Vayssieres, J. R. Durrant, "Artificial photosynthesis for solar water-splitting," *Nat. Photonics*, vol. 6, no. 8, pp. 511–518, 2012, doi: 10.1038/nphoton.2012.175.

[39] A. M. Saleem, V. Desmaris, P. Enoksson, "Performance Enhancement of Carbon Nanomaterials for Supercapacitors," *J. Nanomater.*, vol. 2016, 2016, doi: 10.1155/2016/1537269.

[40] M. Bhardwaj, R. Balasubramaniam, "Uncoupled non-linear equations method for determining kinetic parameters in case of hydrogen evolution reaction following Volmer-Heyrovsky-Tafel mechanism and Volmer-Heyrovsky mechanism," *Int. J. Hydrogen Energy*, vol. 33, no. 9, pp. 2178–2188, 2008, doi: 10.1016/j.ijhydene.2008.02.027.

[41] Y. Li, H. Wang, L. Xie, Y. Liang, G. Hong, H. Dai, "MoS2 nanoparticles grown on graphene: an advanced catalyst for the Hydrogen Evolution Reaction," *J. Am. Chem. Soc.*, vol. 133, pp. 7296–7299, 2011.

[42] M. Zeng, L. Yanguang, "Recent Advances in Heterogeneous Electrocatalysts for Hydrogen Evolution Reaction," *J. of Materials Chem. A*, pp. 3971–3978, 2019. Available: www.rsc.org/materialsA.

[43] Y. Matsumoto, E. Sato, "Electrocatalytic properties of transition metal oxides for oxygen evolution reaction," *Mater. Chem.* Phys., vol. 14, pp. 397-426, 1986.

[44] M. T. M. Koper, "Thermodynamic theory of multi-electron transfer reactions: Implications for electrocatalysis," *J. Electroanal. Chem.*, vol. 660, no. 2, pp. 254–260, 2011, doi: 10.1016/j.jelechem.2010.10.004.

[45] H.-Y. Qu, X. He, Y. Wang, S. Hou, "Electrocatalysis for the Oxygen Evolution Reaction in Acidic Media: Progress and Challenges," *Appl. Sci.*, vol. 11, no. 10, p. 4320, 2021, doi: 10.3390/app11104320.

[46] Q. Liu, Z. Hu, M. Chen, C. Zou, H. Jin, S. Wang, S. L. Chou, Y. Liu, S. X. Dou, "The Cathode Choice for Commercialization of Sodium-Ion Batteries: Layered Transition Metal Oxides versus Prussian Blue Analogs," *Adv. Funct. Mater.*, vol. 30, no. 14, 2020, doi: 10.1002/adfm.201909530.

[47] F. Ma, Q. Li, T. Wang, H. Zhang, G. Wu, "Energy storage materials derived from Prussian blue analogues," *Sci. Bull.*, vol. 62, no. 5, pp. 358–368, 2017, doi: 10.1016/j.scib.2017.01.030.

[48] D. Parajuli, A. Kitajima, A. Takahashi, H. Tanaka, H. Ogawa, Y. Hakuta, K. Yoshino, T. Funahashi, M. Yamaguchi, M. Osada, T. Kawamoto, "Application of Prussian blue nanoparticles for the radioactive Cs decontamination in Fukushima region," *J. Environ. Radioact.*, vol. 151, pp. 233–237, 2016, doi: 10.1016/j.jenvrad.2015.10.014.

[49] L. He, Z. Li, C. Guo, B. Hu, M. Wang, Z. Zhang, M. Du, "Bifunctional bioplatform based on NiCo Prussian blue analogue: Label-free impedimetric aptasensor for the early detection of carcino-embryonic antigen and living cancer cells," *Sensors Actuators, B Chem.*, vol. 298, no. July, p. 126852, 2019, doi: 10.1016/j.snb.2019.126852.

[50] J. Yin, Y. Shen, C. Li, C. Fan, S. Sun, Y. Liu, J. Peng, L. Qing, J. Han, "In Situ Self-Assembly of Core–Shell Multimetal Prussian Blue Analogues for High-Performance Sodium-Ion Batteries," *ChemSusChem*, vol. 12, no. 21, pp. 4786–4790, 2019, doi: 10.1002/cssc.201902013.

[51] W. R. Brant, R. Mongensen, S. Colbin, D. O. Ojwang, S. Schmid, L. Häggström, T. Ericsson, A. Jaworski, A. J. Pell, R. Younesi, "Selective Control of Composition in Prussian White for Enhanced Material Properties," *Chem. Mater.*, vol. 31, no. 18, pp. 7203–7211, 2019, doi: 10.1021/acs.chemmater.9b01494.

[52] Y. Zhao, B. Liang, X. Wei, K. Li, C. Lv, Y. Zhao, "Core-shell heterostructured CuFe@NiFe prussian blue analogue as a novel electrode material for high-capacity and stable capacitive deionization," *J. Mater. Chem. A*, no. 207890, p. 121, 2015, doi: 10.1039/C8TA12433G.Volume.

[53] C. Zhang, Y. Xu, M. Zhou, L. Liang, H. Dong, M. Wu, Y. Yang, Y. Lei, "Potassium Prussian Blue Nanoparticles: A Low-Cost Cathode Material for Potassium-Ion Batteries," *Adv. Funct.*

Mater., vol. 27, no. 4, 2017, doi: 10.1002/adfm.201604307.

[54] W. J. Li, C. Han, G. Cheng, S. L. Chou, H. K. Liu, S. X. Dou, "Chemical Properties, Structural Properties, and Energy Storage Applications of Prussian Blue Analogues," *Small*, vol. 15, no. 32, pp. 1–21, 2019, doi: 10.1002/smll.201900470.

[55] J. Huang, Z. Guo, Y. Ma, D. Bin, Y. Wang, Y. Xia, "Recent Progress of Rechargeable Batteries Using Mild Aqueous Electrolytes," *Small Methods*, vol. 3, no. 1, pp. 1–20, 2019, doi: 10.1002/smtd.201800272.

[56] J. Chen, L. Wei, A. Mahmood, Z. Pei, Z. Zhou, X. Chen, Y. Chen, "Prussian blue, its analogues and their derived materials for electrochemical energy storage and conversion," *Energy Storage Mater.*, vol. 25, no. September 2019, pp. 585–612, 2020, doi: 10.1016/j.ensm.2019.09.024.

[57] B. Wang, Y. Han, X. Wang, N. Bahlawane, H. Pan, M. Yan, Y. Jiang, "Prussian Blue Analogs for Rechargeable Batteries," *iScience*, vol. 3, pp. 110–133, 2018, doi: 10.1016/j.isci.2018.04.008.

[58] F. Herren, P. Fischer, A. Ludi, "Neutron diffraction study of prussian blue, Fe4[Fe(CN)6]3xH2O. Location of water molecules and long-range magnetic order," *inorg. Chem.*, 19, pp. 956–959, 1980.

[59] J. Wu, J. Song, K. Dai, Z. Zhuo, L. A. Wray, G. Liu, Z. X. Shen, R. Zeng, Y. Lu, W. Yang, "Modification of Transition-Metal Redox by Interstitial Water in Hexacyanometalate Electrodes for Sodium-Ion Batteries," *J. Am. Chem. Soc.*, vol. 139, no. 50, pp. 18358–18364, 2017, doi: 10.1021/jacs.7b10460.

[60] H. W. Lee, R. Y. Wang, M. Pasta, S. W. Lee, N. Liu, Y. Cui, "Manganese hexacyanomanganate open framework as a high-capacity positive electrode material for sodium-ion batteries," *Nat. Commun.*, vol. 5, pp. 1–6, 2014, doi: 10.1038/ncomms6280.

[61] F. Jellinek, "Transition metal chalcogenides. relationship between chemical composition, crystal structure and physical properties," *React. Solids*, vol. 5, no. 4, pp. 323–339, 1988, doi: 10.1016/0168-7336(88)80031-7.

[62] M. A. Islam, J. H. Kim, A. Schropp, H. Kalita, N. Choudhary, D. Weitzman, S. I. Khondaker, K. H. Oh, T. Roy, H. S. Chung, Y. Jung, "Centimeter-Scale 2D van der Waals Vertical Heterostructures Integrated on Deformable Substrates Enabled by Gold Sacrificial Layer-Assisted Growth," *Nano Lett.*, vol. 17, no. 10, pp. 6157–6165, 2017, doi: 10.1021/acs.nanolett.7b02776.

[63] S. Wang, J. Zhao, H. Yang, C. Wu, F. Hu, H. Chang, G. Li, D. Ma, D. Zou, M. Huang, "Bottom-up synthesis of WS2 nanosheets with synchronous surface modification for imaging guided tumor regression," *Acta Biomater.*, vol. 58, pp. 442–454, 2017, doi:

10.1016/j.actbio.2017.06.014.

[64] C. Yim, V. Passi, M. C. Lemme, G. S. Duesberg, C. O. Coiláin, E. Pallecchi, D. Fadil, N. McEvoy, "Electrical devices from top-down structured platinum diselenide films," *npj 2D Mater. Appl.*, vol. 2, no. 1, 2018, doi: 10.1038/s41699-018-0051-9.

[65] A. Y. S. Eng, A. Ambrosi, Z. Sofer, P. Šimek, M. Pumera, "Electrochemistry of transition metal dichalcogenides: Strong dependence on the metal-to-chalcogen composition and exfoliation method," *ACS Nano*, vol. 8, no. 12, pp. 12185–12198, 2014, doi: 10.1021/nn503832j.

[66] T. P. Nguyen, S. Choi, J. M. Jeon, K. C. Kwon, H. W. Jang, S. Y. Kim, "Transition Metal Disulfide Nanosheets Synthesized by Facile Sonication Method for the Hydrogen Evolution Reaction," *J. Phys. Chem. C*, vol. 120, no. 7, pp. 3929–3935, 2016, doi: 10.1021/acs.jpcc.5b12164.

[67] Y. Zhang, Y. Yao, M. G. Sendeku, L. Yin, X. Zhan, F. Wang, Z. Wang, J. He, "Recent Progress in CVD Growth of 2D Transition Metal Dichalcogenides and Related Heterostructures," *Adv. Mater.*, vol. 31, no. 41, pp. 1–30, 2019, doi: 10.1002/adma.201901694.

[68] S. P. Lonkar, V. V. Pillai, S. M. Alhassan, " Scalable solid-state synthesis of MoS 2 –NiS 2 /graphene nanohybrids as bifunctional electrocatalysts for enhanced overall water splitting ," *Mater. Adv.*, vol. 1, no. 4, pp. 794–803, 2020, doi: 10.1039/d0ma00192a.

[69] Q. Lu, Y. Yu, Q. Ma, B. Chen, H. Zhang, "2D Transition-Metal-Dichalcogenide-Nanosheet-Based Composites for Photocatalytic and Electrocatalytic Hydrogen Evolution Reactions," *Adv. Mater.*, vol. 28, no. 10, pp. 1917–1933, 2016, doi: 10.1002/adma.201503270.

[70] X. Zhang, G. Ma, J. Wang, "Hydrothermal synthesis of two-dimensional MoS2 and its applications," *Tungsten*, vol. 1, no. 1, pp. 59–79, 2019, doi: 10.1007/s42864-019-00014-9.

[71] J. Yi, X. She, Y. Song, M. Mao, K. Xia, Y. Xu, Z. Mo, J. Wu, H. Xu, H. Li, "Solvothermal synthesis of metallic 1T-WS2: A supporting co-catalyst on carbon nitride nanosheets toward photocatalytic hydrogen evolution," *Chem. Eng. J.*, vol. 335, no. October 2017, pp. 282–289, 2018, doi: 10.1016/j.cej.2017.10.125.

[72] B. Luo, G. Liu, L. Wang, "Recent advances in 2D materials for photocatalysis," *Nanoscale*, vol. 8, no. 13, pp. 6904–6920, 2016, doi: 10.1039/c6nr00546b.

[73] X. Li, E. Khan, G. Chen, X. Sang, J. Lei, D. Passarello, A. D. Oyedele, D. Zakhidov, K. W. Chen, Y. X. Chen, S. H. Hsieh, K. Fujisawa, R. R. Unocic, K. Xiao, A. Salleo, M. F. Toney, C. H. Chen, E. Kaxiras, M. Terrones, B. I. Yakobson, A. R. Harutyunyan, "Surfactant-Mediated Growth and Patterning of Atomically Thin Transition Metal Dichalcogenides," *ACS Nano*, vol. 14, no. 6, pp. 6570–6581, 2020, doi: 10.1021/acsnano.0c00132.

[74] G. Han, S. R. Popuri, H. F. Greer, J. W. G. Bos, W. Zhou, A. R. Knox, A. Montecucco, J. Siviter, E. A. Man, M. Macauley, D. J. Paul, W. Li, M. C. Paul, M. Gao, T. Sweet, R. Freer, F. Azough, H. Baig, N. Sellami, T. K. Mallick, D. H. Gregory, "Facile surfactant-free synthesis of p-type snse nanoplates with exceptional thermoelectric power factors," *Angew. Chemie - Int. Ed.*, vol. 55, no. 22, pp. 6433–6437, 2016, doi: 10.1002/anie.201601420.

[75] A. Sobhani, M. Salavati-Niasari, "Transition metal selenides and diselenides: Hydrothermal fabrication, investigation of morphology, particle size and and their applications in photocatalyst," *Adv. Colloid Interface Sci.*, vol. 287, p. 102321, 2021, doi: 10.1016/j.cis.2020.102321.

[76] A. Sobhani, M. Salavati-Niasari, "Synthesis and characterization of a nickel selenide series via a hydrothermal process," *Superlattices Microstruct.*, vol. 65, pp. 79–90, 2014, doi: 10.1016/j.spmi.2013.10.030.

[77] X. Jiang, H. Gong, Q. Liu, M. Song, C. Huang, "In situ construction of NiSe/Mn0.5Cd0.5S composites for enhanced photocatalytic hydrogen production under visible light," *Appl. Catal. B Environ.*, vol. 268, no. September 2019, p. 118439, 2020, doi: 10.1016/j.apcatb.2019.118439.

[78] M. R. Gao, Z. Y. Lin, T. T. Zhuang, J. Jiang, Y. F. Xu, Y. R. Zheng, S. H. Yu, "Mixed-solution synthesis of sea urchin-like NiSe nanofiber assemblies as economical Pt-free catalysts for electrochemical H 2 production," *J. Mater. Chem.*, vol. 22, no. 27, pp. 13662–13668, 2012, doi: 10.1039/c2jm31916k.

[79] J. Bekker, V. Alberts, M. J. Witcomb, "Influence of selenization techniques on the reaction kinetics of chalcopyrite thin films," *Thin Solid Films*, vol. 387, no. 1–2, pp. 40–43, 2001, doi: 10.1016/S0040-6090(01)00797-0.

[80] Z. Zheng, T. Zhang, J. Yao, Y. Zhang, J. Xu, G. Yang, "Flexible, transparent and ultra-broadband photodetector based on large-area WSe2 film for wearable devices," *Nanotechnology*, vol. 27, no. 22, pp. 1–11, 2016, doi: 10.1088/0957-4484/27/22/225501.

[81] Y. Z. Chen, H. Medina, T. Y. Su, J. G. Li, K. Y. Cheng, P. W. Chiu, Y. L. Chueh, "Ultrafast and low temperature synthesis of highly crystalline and patternable few-layers tungsten diselenide by laser irradiation assisted selenization process," *ACS Nano*, vol. 9, no. 4, pp. 4346–4353, 2015, doi: 10.1021/acsnano.5b00866.

[82] M. Wan, Y. Tang, L. Wang, X. Xiang, X. Li, K. Chen, L. Xue, W. Zhang, Y. Huang, "Core-shell hexacyanoferrate for superior Na-ion batteries," *J. Power Sources*, vol. 329, pp. 290–296, 2016, doi: 10.1016/j.jpowsour.2016.08.059.

[83] Y. Z. Chen, H. Medina, T. Y. Su, J. G. Li, K. Y. Cheng, P. W. Chiu, Y. L. Chueh, "Ultrafast and

low temperature synthesis of highly crystalline and patternable few-layers tungsten diselenide by laser irradiation assisted selenization process," *ACS Nano*, vol. 9, no. 4, pp. 4346–4353, 2015, doi: 10.1021/acsnano.5b00866.

[84] P. Kubelka, F. Munk, "An article on optics of paint layers," *Z. Tech. Phys.*, vol. 12, no. 1930, pp. 593–601, 1931.

[85] G. P. Joshi, N. S. Saxena, R. Mangal, A. Mishra, T. P. Sharma, "Band gap determination of Ni-Zn ferrites," *Bull. Mater. Sci.*, vol. 26, no. 4, pp. 387–389, 2003, doi: 10.1007/BF02711181.

[86] M. Rani, Rachna, U. Shanker, "Metal hexacyanoferrates nanoparticles mediated degradation of carcinogenic aromatic amines," *Environ. Nanotechnology, Monit. Manag.*, vol. 10, no. April, pp. 36–50, 2018, doi: 10.1016/j.enmm.2018.04.005.

[87] S. Wang, P. He, M. He, L. Jia, N. Chen, M. Dong, H. Liu, X. Wang, Y. Zhang, L. Zhou, J. Gao, H. Lei, F. Dong, "Content-dependent electroactivity enhancement of nickel hexacyanoferrate/multi-walled carbon nanotubes electrocatalyst: Cost-efficient construction and promising application for alkaline water splitting," *Int. J. Hydrogen Energy*, vol. 45, no. 4, pp. 2754–2764, 2020, doi: 10.1016/j.ijhydene.2019.11.159.

[88] L. Huang, X. Ge, S. Dong, "A facile conversion of a Ni/Fe coordination polymer to a robust electrocatalyst for the oxygen evolution reaction," *RSC Adv.*, vol. 7, no. 52, pp. 32819–32825, 2017, doi: 10.1039/c7ra04280a.

[89] J. Qiao, F. Song, J. Hu, D. Huo, J. Yuan, J. Shen, L. Niu, A. J. Wang, "Mesoporous spinel NiFe oxide cubes as advanced electrocatalysts for oxygen evolution," *Int. J. Hydrogen Energy*, vol. 44, no. 31, pp. 16368–16377, 2019, doi: 10.1016/j.ijhydene.2019.04.259.